ADVANCED FUNCTIONAL MATERIALS
www.afm-journal.de

Metal Boride-Based Catalysts for Electrochemical Water-Splitting: A Review

Suraj Gupta, Maulik K. Patel, Antonio Miotello, and Nainesh Patel*

Electrocatalytic water-splitting has gained a firm hold in the area of renewable hydrogen production owing to its integrative compatibility with intermittent energy sources. However, wide-scale implementation of this technology demands discovery of new electrode materials that strike a good balance between efficiency, stability, and cost. In the pool of inexpensive electrodes capable of catalyzing hydrogen and oxygen evolution reactions, metal borides/borates have made a big splash in the last decade. However, the research in this family of electrocatalysts remains unorganized owing to the diversity of reports. This review summarizes the past and present research progress in metal borides/borates for electrocatalytic water-splitting. The fundamental reasons for electrochemical behavior in different metal borides/borates are highlighted here, also including some comments regarding erroneous practices in the performance evaluation of metal borides/borates. Various strategies used to enhance the electrocatalytic performance of metal borides/borates are discussed in detail. Different methods evolved over the years for the synthesis of metal borides/borates are also discussed. Finally, an assessment of the commercial viability of metal borides/borates is made and future research directions are suggested.

1. Introduction

The scientific community has fiddled with the idea of producing energy from water for more than a century, since the invention of voltaic pile. Over the course of years, different methods[1] were invented to split the water molecule and generate hydrogen (H_2), which was eventually termed as the "fuel of the future."[2] Electrocatalytic water-splitting was the obvious first choice technology, followed by thermal and photocatalytic decomposition of water. Of these techniques, photocatalytic water-splitting appears to be the most sustainable one but industrial technology based on photocatalytic systems is yet a distant dream mainly because of their inherently low solar to hydrogen (STH) conversion efficiencies.[3–5] In such circumstances, the significance of electrocatalytic water-splitting rises multifold, as it can be coupled to intermittent renewable energy sources (solar, wind, tidal) and deliver a feasible solution to our energy demands.[6,7] Despite being a common-place technology, the global-scale implementation of electrocatalytic water-splitting is not yet achieved, owing to several existing bottlenecks,[7] however not related to conversion efficiency, as in the case of photocatalysis. The most prominent issue with commercial acidic water electrolyzers is the use of expensive noble-metal catalysts (Pt, Ru, Pd, Ir, etc.) as electrode materials.[6–9] These metals are highly efficient and stable in acidic solutions but have high cost and limited reserves in earth's crust that pose great challenges in upscaling them for worldwide implementation.[10] These noble metals are also a major hurdle in competing with the conventional sources in terms of per unit energy cost. In case of alkaline water electrolyzers, these noble-metal catalysts have higher dissolution rates and hence are replaced by Ni, Co, and Fe based electrodes, which are cost-effective and stable but less efficient.[7,11] This creates an anomaly where one has to compromise between efficiency, stability, and cost, when choosing electrodes for acidic/alkaline water electrolyzers. Over the past few decades, a large number of research articles[6,8,12,13] have reported several types of non-noble catalysts that have the potential to replace the present lot of electrodes used in water electrolyzers. However, not many of these alternatives offer a perfect balance between performance, cost and stability. Hence, even now the search for new inexpensive families of materials is the main focus of research, with a hope to discover electrocatalysts capable of solving all the above-listed problems.

Among the different families of non-noble electrocatalysts, the more popular ones for hydrogen evolution reaction (HER) are sulfides,[12,14] selenides,[12,14] phosphides,[12,15] carbides,[12,16] and nitrides[12,16] of transition metals. Most of the catalysts from these families are also active for oxygen evolution reaction (OER),[13,17] in addition to the conventional oxides,[13,17]

Dr. S. Gupta, Dr. M. K. Patel
School of Engineering
University of Liverpool
Liverpool L69 3GH, UK
E-mail: Suraj.Gupta@liverpool.ac.uk
Prof. A. Miotello
Department of Physics
Università degli Studi di Trento
I-38123, Povo, Trento, Italy
Dr. N. Patel
Department of Physics
University of Mumbai
Vidyanagari, Santacruz (East), Mumbai 400098, India
The ORCID identification number(s) for the author(s) of this article can be found under https://doi.org/10.1002/adfm.201906481.

DOI: 10.1002/adfm.201906481

multimetal oxides,[18,19] layered double hydroxides,[20] oxyhydroxides,[21] and perovskites.[13,18] In addition to these, there has been the family of transition-metal borides/borates that have garnered enormous interest in the recent past. Though transition-metal borides (TMBs) have been used for water electrolysis since many decades, they were not really seen as potential candidates to replace noble metal catalysts, until recently. Indeed, in 2009, the group of Daniel Nocera reported in situ formed Co[22] and Ni[23] borates as analogous catalysts to Co phosphate,[24] for near-neutral water-splitting. Later, the groups of Hu[25] and Patel[26] reported development of Mo boride and Co boride, respectively, for electrocatalytic water splitting. Following these reports, transition-metal borides/borates[27–32] were developed using various techniques and were used extensively for water-splitting reactions, in different pH solutions. Here, we would like to inform the readers that usually boron-based catalysts that are developed in situ using electrodeposition are referred to as "borates" (denoted as M–B_i, M = metal) while those catalysts prepared by any other technique are referred to as "borides" (denoted as M–B). Over the past 5–6 years, a lot of studies have been carried out on borides/borates with remarkable results, presenting new possibilities in search for non-noble electrocatalysts. The electrochemical performance, stability and other important properties of all the metal borides reported so far are enlisted in **Table 1** while that of metal borates are listed in **Table 2**. However, there are a lot of aspects that are not yet understood completely about borides/borates. For instance, the occurrence of reverse electron transfer[26] in amorphous Co and Ni borides is well-established, but the chemistry behind this phenomenon is not clear looking at electronegativity of metals (Co and Ni) and boron. In some other borides,[30] electrocatalytic activity varies by varying the proportion of boron in the sample, but this is not a general trend in all borides. The reasons for improvement in electrochemical performance by inclusion of secondary and ternary elements are also not known, in most cases. There are also some issues related to the synthesis of pure phase materials, especially Mo based borides.[33,34] There have been some incisive reports[28,35,36] that tried to gain fundamental understanding of some of the materials belonging to this family, but these efforts are still insufficient and demand better research approaches. The growing interest in boride-based electrocatalysts, combined with the urge to gather understanding of the reported materials, fully justifies a comprehensive review to explore this exciting family of catalysts.

The present review summarizes the various studies carried out using metal boride/borate catalysts for electrocatalytic water-splitting. An effort is made to understand the unique properties possessed by different catalysts belonging to the boride family that render them suitable for electrochemical reactions. Various theories explaining the role of boron in catalyzing HER and OER are also discussed. The review also categorizes the various material-engineering strategies used to enhance the performance of boride catalysts. In later sections, different synthesis methods adopted for these materials are discussed elaborately. A holistic graphical overview of the material-engineering and synthesis strategies presented in this review is shown in **Figure 1**. The potential application of these materials as cocatalysts for enhancing the photocatalytic rates is also highlighted along with the viability of this family for industrial development. Finally,

Suraj Gupta is currently appointed as a Commonwealth Rutherford Fellow at the School of Engineering, University of Liverpool, UK. He received his doctoral degree from University of Mumbai, India in 2016. Following his doctorate, he worked as a National Postdoctoral Fellow at the Department of Chemical Engineering, Indian Institute of Technology Bombay, India (2017–2018) and then moved to Liverpool. His present research is focused on development of nanocatalysts for hydrogen production by different renewable techniques, mainly electrocatalytic and photocatalytic water-splitting.

Antonio Miotello graduated in physics from the University of Padova and after obtaining the position of associate professor, he moved to University of Trento where now he is full professor at the Department of Physics. Here, he was also director of the department and is head of "IdEA (Hydrogen, Energy, Environment)" laboratory dedicated to material science for production of new materials relevant in the energy and environmental fields. The research activity has also allowed the development of patents for industrial applications in the field of solar concentration and coating of materials operating in extreme pressure and temperature conditions.

Nainesh Patel is presently working as an Assistant Professor at the Department of Physics, University of Mumbai under the Faculty Recharge Programme of the Indian Government, since 2014. He completed his doctorate from University of Trento, Italy (2007) and then worked as a postdoctoral researcher at University of Trento from 2007 to 2010. He was then appointed as a senior researcher at the University of Trento from 2011 to 2014. His current research is in field of catalyst materials for energy and environment.

Table 1. Summary of the electrochemical parameters for all the metal boride-based catalysts reported in literature. The table also includes some of the representative catalysts from other non-noble electrocatalyst families, along with IrO_2 and RuO_2, as represented in Figure 18. PBS = phosphate buffered saline (pH 7); KPi = potassium phosphate buffer (pH 7).

Catalyst	Substrate used	Electrolyte	Loading amount [mg cm^{-2}]	Overpotential [mV]		Tafel slope [mV dec^{-1}]		Stability and recyclability		Structure
				HER	OER	HER	OER	HER	OER	
Mo–B[25]	Carbon paste	1 M H_2SO_4	2.50	≈225 (20 mA cm^{-2})	–	55	–	48 h	–	Crystalline
		1 M KOH	2.30	≈240 (20 mA cm^{-2})	–	59	–	48 h	–	
Co–P–B/rGO[54]	GC	0.1 M PBS	0.28	639 (10 mA cm^{-2})	400 (10 mA cm^{-2})	82	68	2.7 h	2.7 h	Partially crystalline
Co–B pellet[26]	None	0.5 M KPi	–	251 (10 mA cm^{-2})	–	75	–	40 h, 1000 cycles	–	Amorphous
Ni–B[27]	GC	1 M $HClO_4$	1.00	132 (20 mA cm^{-2})	–	53, 112	–	8 h	–	Amorphous
		1 M KOH		194 (20 mA cm^{-2})	–	–	–	8 h	–	
Co_2B[28]	GC	0.1 M KOH	0.21	328 (10 mA cm^{-2})	380 (10 mA cm^{-2})	136.2, 177	45	–	60 h, 5000 cycles	Crystalline
Co–Ni–B[47]	GC	0.5 M KPi	2.10	170 (10 mA cm^{-2})	–	51	–	45 h, 1000 cycles	–	Amorphous
		1 M NaOH		133 (10 mA cm^{-2})	–	121	–	45 h, 1000 cycles	–	
Co–B[47]	GC	0.5 M KPi	2.10	197 (10 mA cm^{-2})	–	71	–	–	–	Amorphous
		1 M NaOH		166 (10 mA cm^{-2})	–	–	–	–	–	
NiB_x film[29]	Cu foil	0.5 M H_2SO_4	1.40	45 (10 mA cm^{-2})	–	43	–	42 h	–	Amorphous
		1 M PBS		54 (10 mA cm^{-2})	–	77	–	20 h, 2000 cycles	–	
		1 M KOH		135 (10 mA cm^{-2})	–	88	–	20 h	–	
Ni–B[85]	Ni foam	1 M KOH	12.30	125 (20 mA cm^{-2})	360 (100 mA cm^{-2})	93	76	10 h	10 h	Amorphous
MoB_2[30]	Carbon sheet	0.5 M H_2SO_4	0.20–0.30	230 (2.5 mA cm^{-2})	–	75	–	1000 cycles	–	Crystalline
Co_2B–$CoSe_2$[108]	GC	1 M KOH	0.40	300 (10 mA cm^{-2})	320 (10 mA cm^{-2})	76	56	30 h	–	Amorphous
Co–B–NCNT[98]	GC	0.1 M KOH	0.21	–	370 (10 mA cm^{-2})	–	–	–	51 h	Crystalline
Co–Mo–B[50]	GC	0.5 M KPi	2.10	96 (10 mA cm^{-2})	–	56	–	40 h, 5000 cycles	–	Nanocrystalline
		1 M NaOH		66 (10 mA cm^{-2})	320 (10 mA cm^{-2})	67	155	40 h, 5000 cycles	10 h, 1000 cycles	
Co–Ni–B[51]	Ni foam	KOH	–	205 (10 mA cm^{-2})	313 (10 mA cm^{-2})	–	120	12 h	12 h	Partially crystalline
Co–W–B[52]	Ni foam	1 M KOH	–	98 (10 mA cm^{-2})	360 (10 mA cm^{-2})	83	–	12 h	–	Nanocrystalline
Co–B[139]	Carbon paper	1 M KOH	2.56	–	340 (10 mA cm^{-2})		63			Crystalline
Co_2B[139]				109 (10 mA cm^{-2})	287 (10 mA cm^{-2})	–	50.7	–	12 h, 1000 cycles	Crystalline
Co_3B[139]				–	312 (10 mA cm^{-2})	–	53	–	–	Crystalline
Co–B[139]	GC	0.1 M KOH	0.20	–	405 (10 mA cm^{-2})	–	–	–	–	–
Co_2B[139]				–	371 (10 mA cm^{-2})	–	–	–	–	–
Co_3B[139]				–	378 (10 mA cm^{-2})	–	–	–	–	–
Co–Fe–B[76]	Cu sheet	1 M KOH	1.20	–	298 (10 mA cm^{-2})	–	62.6	–	12 h	Amorphous
Etched Mo–Al–B[137]	Unsupported	0.5 M H_2SO_4	–	361 (10 mA cm^{-2})	–	–	–	24 h	–	Crystalline

Table 1. Continued.

Catalyst	Substrate used	Electrolyte	Loading amount [mg cm^{-2}]	Overpotential [mV]		Tafel slope [mV dec^{-1}]		Stability and recyclability		Structure
				HER	OER	HER	OER	HER	OER	
FeB_2[53]	GC	1 M KOH	0.20	61 (10 mA cm^{-2})	296 (10 mA cm^{-2})	87.5	52.4	24 h	48 h, 1000 cycles	Crystalline
Fe–Co–Ni–B[75]	GC	1 M KOH	0.30	–	274 (10 mA cm^{-2})	–	38	12 h, 1000 cycles	–	Amorphous
Mo_2B_4[33]	Carbon sheet	0.5 M H_2SO_4	0.60–0.70	270 (3.5 mA cm^{-2})	–	80	–	2000 cycles	–	Crystalline
MoB_2[34]	Carbon sheet	0.5 M H_2SO_4	0.50	154 (10 mA cm^{-2})	–	49	–	1000 cycles	–	Crystalline
Ni–Bi@Ni_3B[79]	GC	1 M KOH	0.30	–	302 (10 mA cm^{-2})	–	52	–	8 h	Partially crystalline
Ni–B@NiO[106]	Cu foil	1 M KOH	1.40	–	296 (10 mA cm^{-2})	–	58	–	60 h	Amorphous
Ni–Fe–B nanochains[109]	GC	0.1 M KOH	0.36	–	350 mV (64 Ag^{-1})	–	40	–	2.7 h	Amorphous
Ni_x–B nanosheets[71]	GC	1 M KOH	0.21	–	380 (10 mA cm^{-2})	–	89	–	60 h	Amorphous
Mo_3B films[140]	Mo foil	0.5 M H_2SO_4	–	249 (20 mA cm^{-2})	–	52	–	15 h, 2500 cycles	–	Crystalline
Ni–Fe–B[113]	GC	1 M KOH	0.20	–	251 (10 mA cm^{-2})	–	43	–	≈3 h	Amorphous
		0.1 M KOH	–	–	316 (10 mA cm^{-2})	–	61	–	≈3 h	
		0.1 M KBi	–	–	436 (10 mA cm^{-2})	–	76	–	≈3 h	
		0.1 M KPi	–	–	550 (5 mA cm^{-2})	–	81	–	≈3 h	
Co–B/porous carbon[96]	GC	1 M KOH	0.16	–	320 (10 mA cm^{-2})	–	75	–	20 h	Amorphous
Co–B[100]	Ni foam	1 M KOH	12.00	110 (10 mA cm^{-2})	315 (10 mA cm^{-2})	96	80	12 h	12 h	Nanocrystalline
Co–B–P nanosheets[59]	Ni foam	1 M KOH	5.00	42 (10 mA cm^{-2})	–	42.1	–	20 h, 1000 cycles	–	Amorphous
Co–Fe–B–O[74]	GC	1 M KOH	0.20	–	263 (10 mA cm^{-2})	–	39	–	–	Amorphous
		0.1 M KOH	–	–	356 (10 mA cm^{-2})	–	–	–	–	
		0.1 M KBi	–	–	460 (10 mA cm^{-2})	–	–	–	–	
		0.1 M KPi	–	–	500 (5 mA cm^{-2})	–	–	–	–	
Co–Ni–B[60]	GC	1 M KOH	≈0.76	–	310 (10 mA cm^{-2})	–	66	–	35 h	Amorphous
Co–Ni–B[61]	Carbon cloth	1 M KOH	0.34	80 (10 mA cm^{-2})	–	88.2	–	36 h, 1000 cycles	–	Amorphous
Co–P–B[55]	Carbon paper	0.5 M H_2SO_4	–	172 (10 mA cm^{-2})	–	68	–	–	–	Amorphous
Fe^{3+} doped $Co_2BO_y(OH)_z$[70]	GC	1 M KOH	0.20	–	308 (10 mA cm^{-2})	–	39	–	12 h	Amorphous
Fe–Ni–B sheets[84]	Ni foam	1 M KOH	1.00	–	237 (10 mA cm^{-2})	–	38	–	12 h, 1000 cycles	Amorphous
Ni_3B–rGO[97]	Carbon paper	1 M KOH	0.20	–	290 (10 mA cm^{-2})	–	88.4	–	12 h	Nanocrystalline
Ni–Fe–B–rGO[114]	GC	1 M KOH	0.20	–	265 (10 mA cm^{-2})	–	58	–	20 h	Crystalline
Co–P–B[58]	GC	1 M NaOH	1.42	145 (10 mA cm^{-2})	290 (10 mA cm^{-2})	38	42	20 h, 1000 cycles	20 h, 500 cycles	Amorphous
Ni_3B[157]	–	0.5 M H_2SO_4	–	79 (10 mA cm^{-2})	–	85.32	–	20 h, 5000 cycles	–	Crystalline
Ni–Co–B/rGO[111]	GC	1 M KOH	–	–	280 (10 mA cm^{-2})	–	56	–	60 h	Crystalline

Table 1. Continued.

Catalyst	Substrate used	Electrolyte	Loading amount [mg cm^{-2}]	Overpotential [mV]		Tafel slope [mV dec^{-1}]		Stability and recyclability		Structure
				HER	OER	HER	OER	HER	OER	
Ni_2B–gC_3N_4[95]	GC	1 M KOH	–	707 (10 mA cm^{-2})	–	221	–	–	–	Amorphous
Ni–Co–B[103]	Ni foam	1 M KOH	4.00	–	300 (10 mA cm^{-2})	–	113	–	55 h	Amorphous
Boronized NiFe[88]	NiFe sheet	1 M KOH	–	–	270 (10 mA cm^{-2})	–	–	–	3000 h	Crystalline
V-doped Co–Ni boride[87]	Ni foam	1 M KOH	–	–	280 (30 mA cm^{-2})	–	101	–	10 h, 1000 cycles	Crystalline
Ni_xB-f-MWCNT[158]	GC	1 M KOH	0.20	116 (10 mA cm^{-2})	286 (10 mA cm^{-2})	70.4	46.3	100 h	100 h	Crystalline
Fe_3Co_7B/CNT[131]	GC	1 M KOH	0.30	–	265 (10 mA cm^{-2})	–	30	–	12 h, 1000 cycles	Amorphous
Co–B nanosheets[159]	Ni foam	1 M KOH	8.00	–	265 (20 mA cm^{-2})	–	55.6	–	10 h, 1000 cycles	Amorphous
Co_2B/Co/N–B–C/B_4C[141]	GC	0.1 M KOH	2.00	220 (10 mA cm^{-2})	300 (10 mA cm^{-2})	105	111	1000 cycles	1000 cycles	Crystalline
IrO_2[152]	GC	1 M KOH	0.15	–	330 (10 mA cm^{-2})	–	52	–	–	–
RuO_2[32]	GC	1 M KOH	0.28	–	305 (10 mA cm^{-2})	–	60	–	–	–
NiFe LDH[160]	Ni foam	1 M KOH	1.00	–	224 (10 mA cm^{-2})	–	52.8	–	50 h	–
Co_4N[156]	CC	1 M KOH	0.82	–	257 (10 mA cm^{-2})	–	44	–	12 h, 1000 cycles	–
Ni_2P[64]	GC	1 M KOH	0.14	–	290 (10 mA cm^{-2})	–	59	–	10 h	–
Co–P/C[65]	GC	1 M KOH	0.71	–	320 (10 mA cm^{-2})	–	71	–	12 h	–
$Ni_{0.8}Fe_{0.2}S_2$[155]	GC	1 M KOH	0.18	–	230 (10 mA cm^{-2})	–	42.6	–	50 h	–
$Ni_{2.0}Mo_{0.26}C$@NCNT[153]	GC	1 M KOH	0.28	–	310 (10 mA cm^{-2})	–	62.7	–	10 h, 1000 cycles	–
$Co_6Mo_6C_2$/NCRGO[154]	GC	1 M KOH	0.14	–	260 (10 mA cm^{-2})	–	50	–	2000 cycles	–

some of the open research challenges are discussed, useful, in our opinion to gain more understanding and further improve the electrochemical performance of metal borides/borates.

2. Origin of Electrochemical Activity in Metal Borides

The complete water-splitting mechanism consists of two half-reactions taking place almost simultaneously, namely, HER and OER, at negative and positive electrodes, respectively.[7,37] The mechanism of splitting water molecules into H_2 and oxygen (O_2) appears simple but proceeds in different ways in different pH solutions.[7] Equations (1–6) represent the water-splitting half-reactions in acidic (Equations (1) and (2)), basic (Equations (3) and (4)), and neutral (Equations (5) and (6)) media.

In acidic medium (e.g., hydrochloric acid)

$$\text{Cathode:}\quad 4H^+ + 4e^- \rightarrow 2H_2 \tag{1}$$

$$\text{Anode:}\quad 2H_2O \rightarrow O_2 + 4H^+ + 4e^- \tag{2}$$

In basic medium (e.g., potassium hydroxide)

$$\text{Cathode:}\quad 4H_2O + 4e^- \rightarrow 2H_2 + 4OH^- \tag{3}$$

$$\text{Anode:}\quad 4OH^- \rightarrow O_2 + 2H_2O + 4e^- \tag{4}$$

In neutral medium (e.g., potassium phosphate buffer)

$$\text{Cathode:}\quad 4H_2O + 4e^- \rightarrow 2H_2 + 4OH^- \tag{5}$$

$$\text{Anode:}\quad 2H_2O \rightarrow O_2 + 4H^+ + 4e^- \tag{6}$$

Irrespective of the electrolyte medium, a catalyst must acquire certain properties that make them suitable for catalyzing the HER and OER. In the following section, some examples, from literature, are elaborately discussed to clarify what gives rise to electrochemical activity in various metal borides.

2.1. Hydrogen Evolution Reaction

Among the two half-reactions of water-splitting, HER is the simpler one constituting a two-step process: 1) adsorption of H_2O

Table 2. Summary of the electrochemical parameters for all the metal borate-based electrocatalysts reported in literature. KBi = potassium borate buffer (pH 9.2).

Catalyst	Substrate used	Electrolyte	Loading amount [mg cm^{-2}]	Overpotential [mV]		Tafel slope [mV dec^{-1}]		Stability and recyclability		Structure
				HER	OER	HER	OER	HER	OER	
Ni–B_i[23]	ITO	0.1 M KBi	–	–	425 (1 mA cm^{-2})	–	59	–	100 cycles	Amorphous
Co–B_i[102]	Graphene foam	0.1 M KBi	1.00–2.00	–	315 (1 mA cm^{-2})	–	59	–	8 h	–
Co–B_i nanosheet-graphene[32]	GC	1 M KOH	0.28	–	290 (10 mA cm^{-2})		53		≈11 h, 1000 cycles	Amorphous
		Phosphate buffer		–	235 (onset)	–	–	–	≈17 h, 1000 cycles	
Co@Co–B_i[31]	Ti mesh	1 M KOH	–	–	327 (10 mA cm^{-2})	–	46	–	5.5 h, 2000 cycles	Crystalline (Co core) amorphous (CoB_i)
	GC		0.20	–	373 (10 mA cm^{-2})	–	–	–	–	
Co–B_i nanosheet array[104]	Ti mesh	0.1 M KBi	1.20	–	469 (10 mA cm^{-2})	–	138	–	25 h, 1000 cycles	Amorphous
		0.5 M KBi		–	400 (10 mA cm^{-2})	–	–	–	–	
Fe–P_i–B_i[57]	Carbon cloth	0.1 M KBi	2.21	–	434 (10 mA cm^{-2})	–	94	–	20 h, 500 cycles	Amorphous
		0.5 M KBi		–	383 (10 mA cm^{-2})	–	–	–	–	
Ni_3N@ Ni–B_i[107]	Ti mesh	0.1 M KBi	1.61	–	405 (10 mA cm^{-2})	–	82	–	–	Crystalline (Ni_3N core) Amorphous (N_iB_i)
		0.5 M KBi	–	265 (10 mA cm^{-2})	382 (10 mA cm^{-2})	190	–	20 h, 1000 cycles	20 h, 1000 cycles	
Ni–B_i nanosheet array[105]	Ti mesh	0.1 M KBi	1.90	–	430 (10 mA cm^{-2})	–	276	–	21 h, 1000 cycles	Amorphous
NiB_i@Ni–B[79]	GC	1 M KOH	0.30	–	364 (10 mA cm^{-2})	–	65	–	4 h	Amorphous (both core and shell)
				–	302 (10 mA cm^{-2})	–	52	–	8 h	Partially crystalline (N_i–B_i shell) Crystalline core (Ni_3B)
Ni–B_i[99]	Carbon cloth	0.1 M KBi	2.30	–	470 (10 mA cm^{-2})	–	107	–	25 h, 1000 cycles	Amorphous
		0.5 M KBi		–	390 (10 mA cm^{-2})	–	–	–	–	
Ni–B_i–P_i[56]	Carbon cloth	0.1 M KBi	2.20	–	440 (10 mA cm^{-2})	–	139	–	23 h, 500 cycles	Amorphous
		0.5 M KBi		–	359 (10 mA cm^{-2})	–	–	–	–	
Ni–Co–B_i[80]	Carbon cloth	0.1 M KBi	2.10	–	388 (10 mA cm^{-2})	–	142	–	≈22 h, 500 cycles	Amorphous
		0.5 M KBi		–	316 (10 mA cm^{-2})	–	97	–	–	

or H^+ species on the cathode (also called Volmer step) and 2) desorption of H_2 from the cathode through chemical (Tafel step) or electrochemical (Heyrovsky step) route (**Figure 2**).[12,38,39] For any material to be a good HER catalyst, it should have some basic characteristics such as a) large number of active sites with optimum electron density to generate moderate bonding strength with adsorbed H atom (Sabatier principle),[40] so that the adsorption or desorption process is not hindered, b) low charge transfer resistance across interface as well as with bottom lying electrode material and c) stability in the electrolyte medium. Based on these parameters, the rationale behind the performance of various electrocatalysts can be explained conveniently. For instance, the supremely high HER performance of Pt is majorly ascribed to its optimum H-bonding strength as

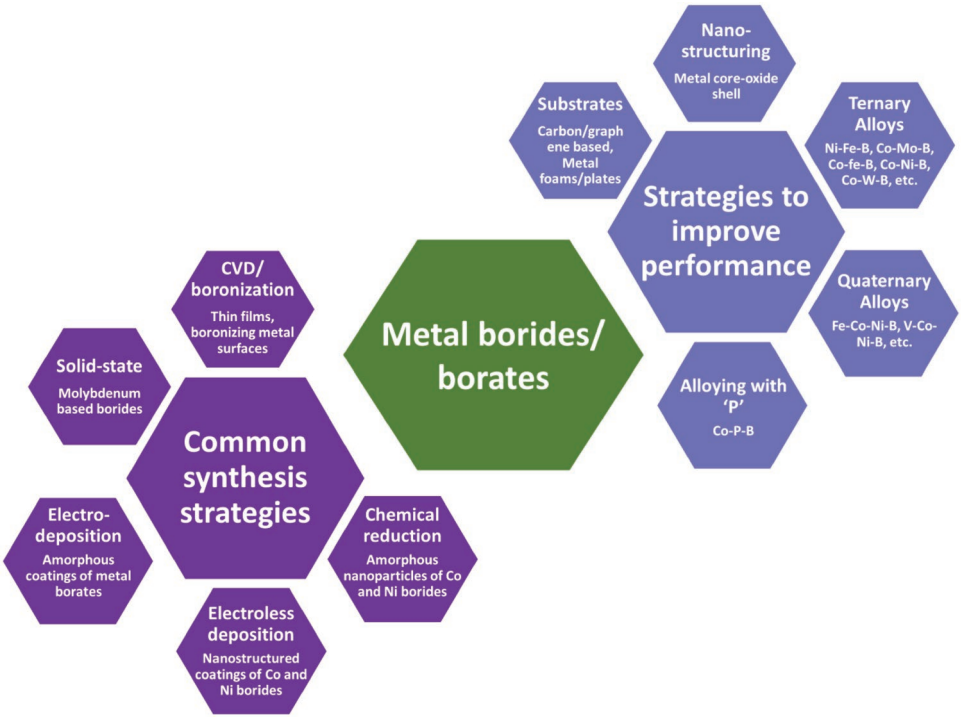

Figure 1. Overview of strategies used to synthesize and improve the performance of metal borides/borates, as discussed in the review.

it sits at the top of the Volcano plot (**Figure 3**a).[41,42] Similarly, electrocatalysts belonging to the sulfide (MoS_2) family show HER activity owing to the highly active sulfur atoms on the Mo edges of MoS_2 planes (Figure 3b).[43,44] In case of phosphides (Ni, Co, and Mo based), higher HER activity is attributed to the "ensemble effect" (also called "ligand effect")[15,45] where the positively charged metal center ($M^{\delta+}$) acts as the hydride acceptor while the negatively charged phosphorous center ($P^{\delta-}$) acts as the proton acceptor, facilitating HER. However, a similar consensus is not yet developed for the family of metal borides.

In case of amorphous metal borides, the most widely accepted reason for higher HER rate was proposed by Patel

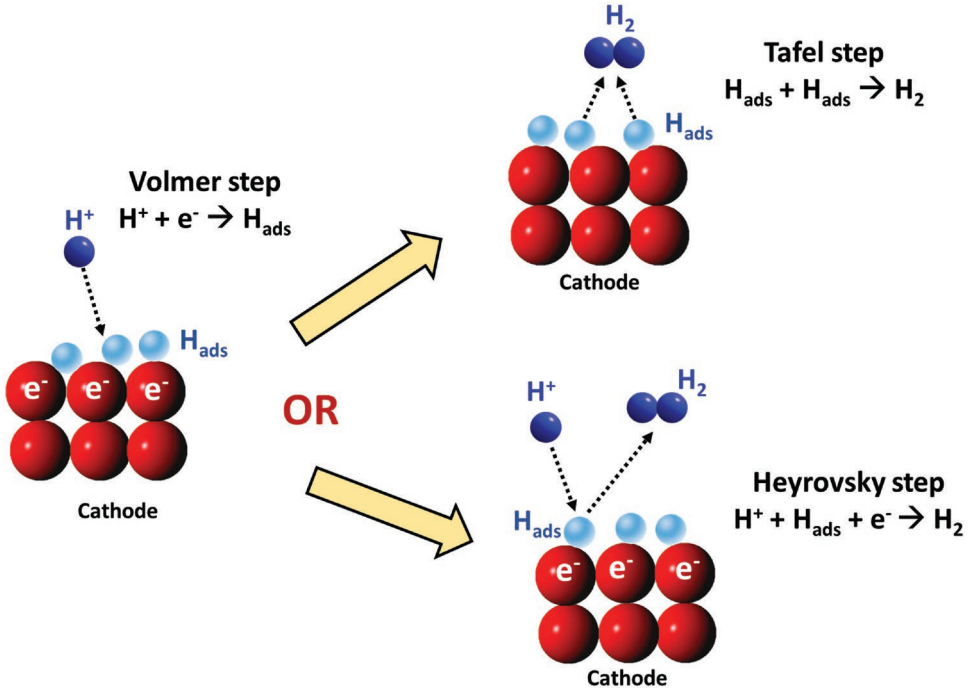

Figure 2. Schematic representing possible reaction routes for HER on a cathode.

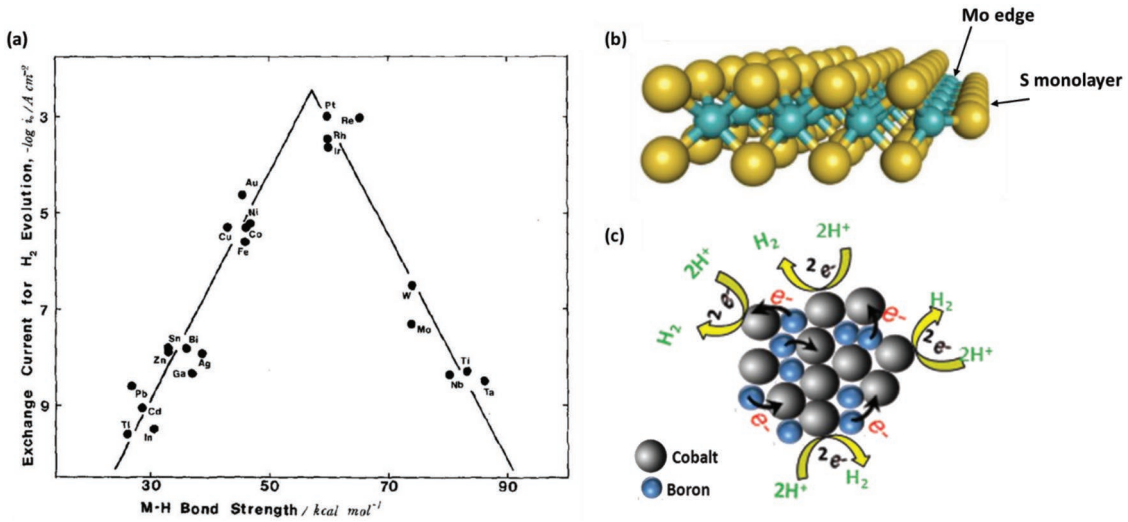

Figure 3. a) Volcano plot for HER on various metals indicating the relation between observed exchange current density and the hydrogen bonding adsorption strength (ΔE_{M-H}). Reproduced with permission.[41] Copyright 1972, Elsevier. b) A model representation of the MoS_2 nanostripe with exposed Mo-edge on its right side covered by sulfur monomers. Adapted with permission.[44] Copyright 2017, Wiley-VCH. c) Schematic illustration of HER in amorphous Co–B cluster. Reproduced with permission.[26] Copyright 2015, Elsevier.

and co-workers for Co–B.[26] The value of Pauling's electronegativity for B (2.01) is higher than that of Co (1.70).[46] Thus, when a compound of Co and B is made (Co–B), the expected electronic interaction will lead to transfer of electrons from Co to B, making the metal site electron deficient. Density functional theory (DFT) studies carried out on crystalline Co–B and Co_2B clusters agree well with this.[26] However, when an amorphous cluster of Co and B is simulated, partial transfer of electron density toward Co metal is observed. This reverse electron transfer phenomenon was also verified by binding energy shift observed in X-ray photo-electron spectroscopy (XPS) data of amorphous Co–B.[26] Owing to this reverse electron transfer, the d-band orbitals of Co are filled with more number of electrons and are expected to act as favorable active sites for facilitating HER (Figure 3c). By donating electrons, B may play a sacrificial role to prevent the oxidation of the metal sites and improve their stability. A number of reports on amorphous Co and Ni based borides agree well with this reverse electron transfer phenomenon being responsible for higher HER rate.[29,47–52]

Though the above model explains the higher HER performance of amorphous metal borides, it is debatable for their crystalline counterparts. For Fe-based boride which exists in crystalline form (Fe_2B and FeB_2), the mechanism of HER was analyzed considering the adsorption of a single H atom on the high index (110) and low index (001) facets (**Figure 4**a).[53] A lower value of Gibbs adsorption energy (ΔG_H) is desired to achieve optimum bonding strength with the adsorbed species. The top B site of the low index surface (001) of FeB_2 showed the lowest ΔG_H value, indicating it to be the main site responsible for HER (Figure 4b). On the other hand, iron-rich Fe_2B showed much higher ΔG_H values on both (001) as well as (110) surfaces when compared to FeB_2, thereby indicating that boron-rich FeB_2 is more likely to show better HER rate, matching well with experimental results. Likewise, Fokwa and co-workers[30] found a boron-dependency on the HER activity of Mo-based borides. They observed that with increasing the boron content, B–B connectivity increases and the structure transforms from less active 0D (Mo_2B with isolated B) to 1D (α-MoB and β-MoB with zigzag B chains) and to most active 2D (MoB_2 with graphene-like B layers) for HER (Figure 4c). DFT calculations were used to determine ΔG_H values for two flat B-surfaces and two puckered B-surfaces of another Mo based boride, i.e., Mo_2B_4 (with same Mo to B ratio as in MoB_2).[33] The binding strength of H atom on flat graphene-like B-surface was much lower than that on puckered phosphorene-like B-surface, making the latter less active for HER (Figure 4d). In fact, H-bonding strength on flat B layer was close to that of Pt (111) surface, suggesting it to be highly active for HER. In Mo_2B_4, domination of less active puckered B layers is observed in contrast to MoB_2 which is made up of flat graphene-like B layers, suggesting MoB_2 to be the more active catalyst. This indicates that development of Mo-based borides with flat graphene-like B layers must be adopted, to obtain the best performance.

The electrocatalytic performance of mono-metal borides improve drastically after incorporation of a second element (examples discussed later).[47,50–52] While most reports just summarize the performance chart, only few of them tried to understand the role of these secondary elements in improving the HER rates. For amorphous Co–Ni–B,[47] the role of Ni was explained by correlating the data obtained from XPS, X-ray absorption near edge structure (XANES) (**Figure 5**a), extended X-ray absorption fine structure (EXAFS) (Figure 5b,c), and DFT calculations. EXAFS fitting depicted that addition of Ni in Co–B rearranges the second shell atomic distribution to form more number of bonds between Co and B. This creates opportunity for transfer of more number of electrons from B to Co and hence improves the HER rate. Inclusion of Mo in Co–B,[50] on the other hand, leads to formation of smaller sized particles, creating more number of active sites for HER. There are other ternary catalysts formed by inclusion of phosphorous (P) in the metal boride (e.g., Co–P–B,[54,55] Ni–P–B,[56] Fe–P–B,[57] etc.). Here, P plays a crucial role in modifying the electronic structure

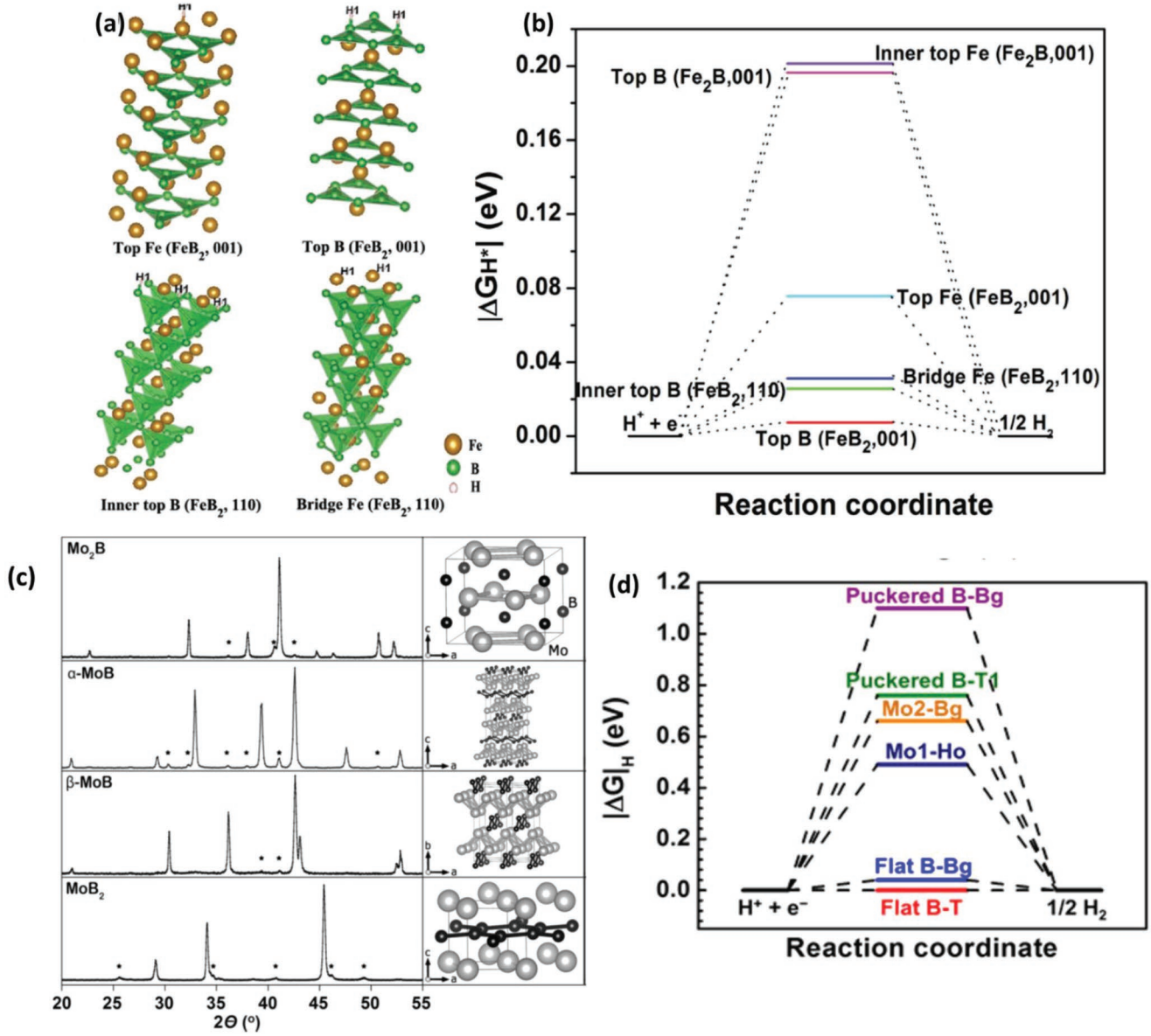

Figure 4. a) A model representing the high index (110) and low index (001) H adsorption sites of FeB_2. b) Calculated free-energy diagram for HER over (110) and (001) surfaces of FeB_2 and Fe_2B. Reproduced with permission.[53] Copyright 2017, Wiley-VCH. c) X-ray diffraction patterns and corresponding crystal structures of Mo_2B, α-MoB, β-MoB, and MoB_2. (*) indicates the peaks of impurity phases. Reproduced with permission.[30] Copyright 2017, Wiley-VCH. d) Calculated free-energy diagram for HER over different surfaces of Mo_2B_4, indicating flat B layers to be the most preferred sites. Reproduced with permission.[33] Copyright 2017, American Chemical Society.

of the base metal boride and facilitating HER. Patel and coworkers[58] found a unique interplay in Co–P–B catalyst where electrons were transferred from B to Co and Co to P, thereby modulating the electron density of Co for moderate H-adsorption. Another report proposed a plausible reaction mechanism for HER on Co–B–P as schematically depicted in Figure 5d.[59] In the first step, an interaction between $Co^{\delta+}$ and O^{2-}, combined with that between $P^{\delta-}$ and H^+ enhances the adsorption of H_2O and weakens the HO—H bond, leading to dissociation of adsorbed H_2O. In the next step, H^+ adsorbed on $P^{\delta-}$ transfers to nearby $Co^{\delta+}$ and combine with H from adsorbed OH^- to form H_2 molecule. The interaction between Co and H is too strong in Co–P, but in Co–P–B, the bonding is optimized owing to the transfer of electrons from B to Co, thereby increasing HER activity. Apart from these elements, HER activity of many other ternary catalysts has been reported,[52,60,61] but no efforts were taken to understand the role of incorporated metals.

2.2. Oxygen Evolution Reaction

When compared to HER, OER is a comparatively sluggish reaction involving multielectron transfer making it more energy intensive.[13] Different possible routes for OER in acidic and

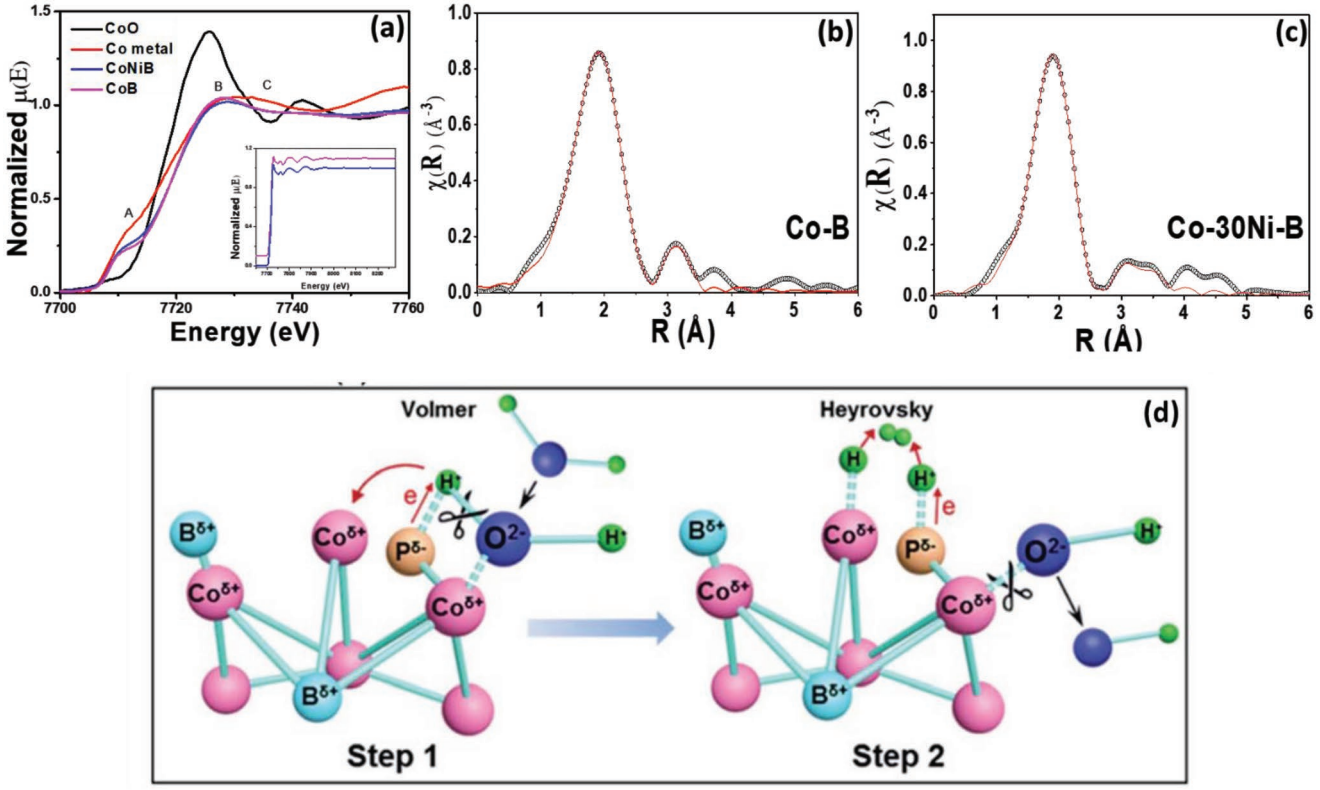

Figure 5. a) XANES spectra of Co–B, Co–Ni–B, and reference Co samples. Fourier transformed Co K edge EXAFS spectra of b) Co–B and c) Co–30Ni–B. Reproduced with permission.[47] Copyright 2016, Elsevier. d) Schematic illustration of HER mechanism on Co–B–P, portraying the role of each element sites. Reproduced with permission.[59] Copyright 2018, Royal Society of Chemistry.

basic medium are reported by Matsumoto and Sato,[62] and later by Hong et al.,[63] and involves reaction intermediates such as OH* and OOH*. The formation of these intermediates on the electrode surface is a prerequisite for OER and can serve as the rate-limiting step. Thus, materials that can readily form these surface species with optimum bonding energies are considered as ideal OER catalysts. Owing to these characteristics, oxides of Ru and Ir have been conventionally used for OER in acidic as well as alkaline media.[13] Apart from these, layered hydroxides, metal and mixed-metal oxides have been extensively reported as low-cost alternatives for RuO_2 and IrO_2.[13,17] For nonoxide catalysts such as metal phosphides[64,65] and sulfides,[66,67] OER proceeds via in situ formation of surface oxides/hydroxides that catalyze the reaction. Recently, Mullins and co-workers[68] presented an excellent analysis of the degree of oxidation in metal chalcogenides, pnictides, and carbides during OER and summarized the various theories for their electrochemical activity. In case of metal borides as well, OER proceeds in a similar fashion by forming surface oxide/hydroxide species.[28,50,69,70] Operando X-ray absorption spectroscopy (XAS) studies on Ni_xB[71] showed that during OER, Ni–B core remains intact while the surface oxidation state changes from Ni^{2+} to Ni^{3+} (**Figure 6**a,b), thus giving direct evidence of the formation of surface NiOOH layer. Similarly, for Ni borate (NiB_i) films, different groups[36,72] reported XAS data indicating a similar increment in the oxidation state of Ni to Ni^{4+}, under oxidation potential. When probed using in situ O–K edge XAFS,[73] the peak corresponding to formation of NiO_6 octahedra increases (Figure 6c) under applied potential, suggesting structural change from β-NiOOH to γ-NiOOH, matching with the above results. When the potential direction was reversed, it was observed that the reduction of NiO_6 octahedra took place majorly at the edges while the bulk reduced rather gradually. However, the OER current was suppressed considerably (Figure 6d), suggesting that the edges of NiO_6 octahedra are the dominant active sites in NiB_i thin films (schematically represented in Figure 6e). Formation of similar CoOOH and FeOOH species on the surface of Co and Fe based borides,[70,74–78] respectively, after OER tests were reported by many authors as responsible for enhancing the OER performance.

For OER, although the surface oxidation state is a major factor, there can be several other factors contributing to the performance of a catalyst, considering the complexity of the process as a whole. Here, we look at some examples from literature that report various other reasons contributing to the OER performance in different metal borides. XAS studies on as prepared and annealed Co_2B[28] indicated presence of strain induced by B on the crystal lattice of Co, originating from the chemical interaction and hybridization of B 2p states with metal d orbitals. This lattice strain reduces the energy barrier for oxidation of Co and leads to formation of OOH* intermediates more easily, thereby improving the OER rate. The effect of crystallinity on OER was demonstrated as partially crystalline NiB_i@NiB catalyst showcased better OER rate than amorphous

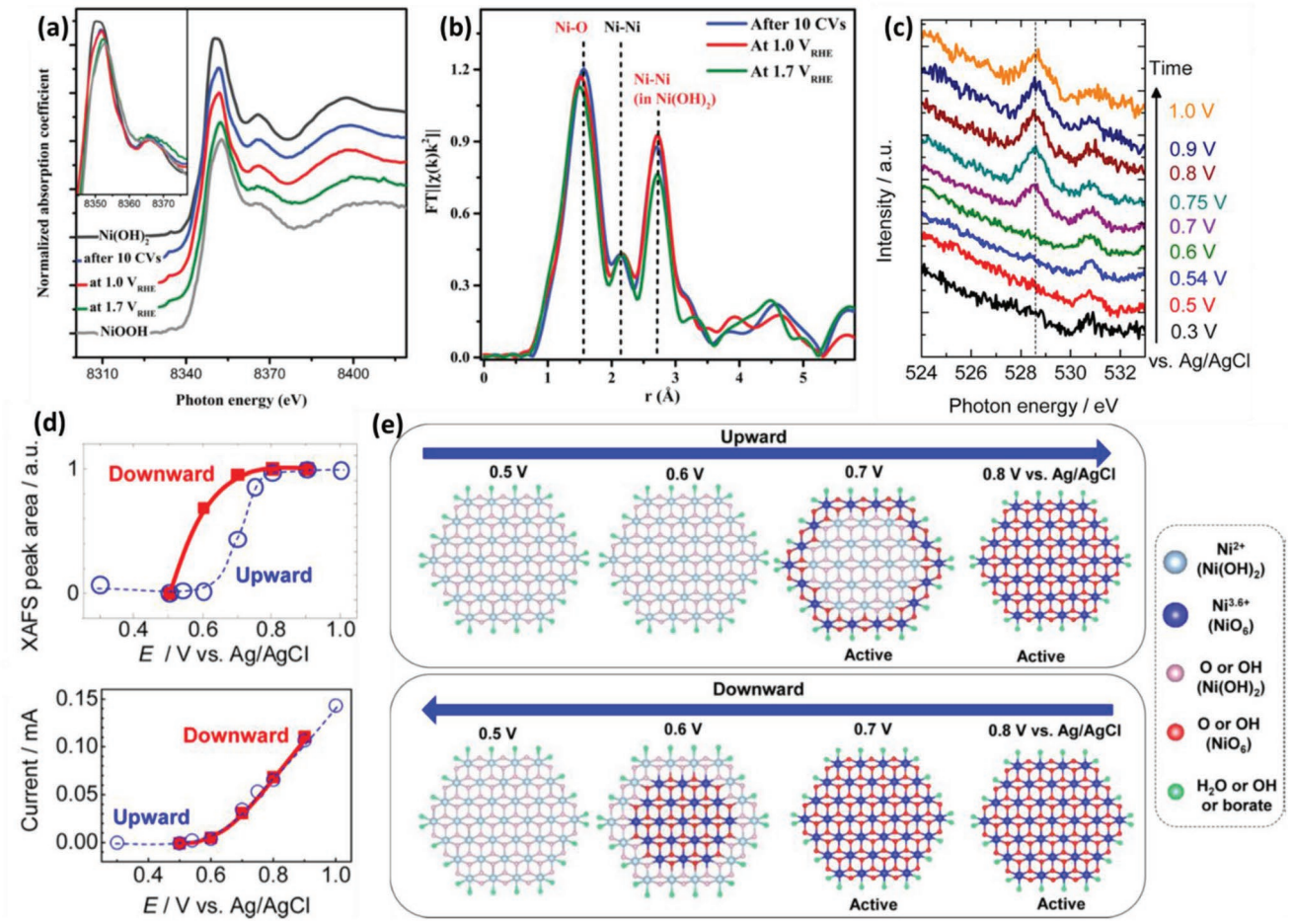

Figure 6. Operando a) XANES and b) EXAFS spectra of Ni_xB-300 acquired at different oxidative potentials. Reproduced with permission.[71] Copyright 2017, Wiley-VCH. c) In situ O K-edge XAFS spectra for Ni–B_i catalyst, indicating formation of NiO_6 phase with increasing oxidative potential. d) Variation in OER currents and XAFS peak area for NiB_i with variation in electrode potential. e) Schematic representing the changes in chemistry of Ni–B_i electrocatalyst during OER by upward and downward sweeping of the electrode potentials. Reproduced with permission.[73] Copyright 2015, American Chemical Society.

as well as completely crystalline NiB_i@NiB.[79] In another work,[76] it was observed that during cyclic voltammetry (CV) measurements of Co–Fe–B catalyst, the Co^{2+}/Co^{3+} oxidation peak shifts to higher potential, with increasing Fe content, indicating a strong electronic interaction between Co and Fe. By calculating the amount of charge transformation, it was shown that the optimized catalyst (Co–2Fe–B) contained more number of Co species in higher oxidation states, which is active for initiating OER. Xue et al.[70] probed Fe^{3+} doped $Co_2BO_y(OH)_z$ using ^{57}Fe Mossbauer spectroscopy and proposed that when the doping amount of Fe^{3+} is 30%, it modifies the electronic structure and modulates the hydroxyl adsorption ability of the catalyst, thereby facilitating OER. However, when the doping concentration of Fe^{3+} increases beyond 30%, phase separation takes place and separate crystalline phases of $Fe(OH)_3$ and $Fe_5O_7(OH)\cdot 4H_2O$ are formed, which lead to decrease in OER performance. For Ni–Co–B_i,[80] DFT calculations suggested that addition of Ni substitutes the Co atom and the extra valence electron (of Ni) is transferred to the lattice O ions, which then pass on some electrons to the binding Co ions via Co–O bonds. Bader charge analysis confirms transfer of ≈0.072 e^- to Co from the surrounding O ions, resulting in slightly reduced Co ions. These Co ions become preferred sites for interacting strongly with the OER intermediates (O* and OOH*), thereby decreasing the ΔG for oxidation and enhancing OER activity.

From the above discussion, it becomes clear that there can be several reasons for improvement of the OER rate in multimetal borides/borates, with contributions from the constituent metals. However, in monometal borides/borates, the higher OER rate is only explained in context of surface metal oxide/hydroxide formation, with no clarity over the role of boron, unlike HER where the role of boron as a "sacrificial" electron donor is clearly explained (in Section 2.1). Recently, Masa and Schuhmann[81] reviewed the role of nonmetals (N, P, S, Se) and metalloids (B, C, As, Te) in improving the OER activity of Co and Ni-based electrocatalysts. For Co and Ni borides, they suggested a possibility that the surface boron species leach out in the electrolyte, creating pores on the catalyst surface and increasing the electrochemical surface area (ECSA), thereby improving OER rate. We suggest that this possibility must be experimentally verified by detecting the concentration of boron

in the electrolyte after OER test. The review also emphasized that metal oxide/hydroxide species act as the active center, while boron facilitates OER by modulating the interaction energies of the reaction intermediates. In our recent report on amorphous/nanocrystalline Co–B films,[78] we proposed that boron helps in preventing complete oxidation of Co (by donating electrons) to form stable oxides, thereby facilitating formation of intermediate oxide/hydroxide species more easily, as compared to Co oxides. Looking at all these theories, it can be said with certainty that boron does not act as the active site for OER but does play a crucial role in formation of the reaction intermediates.

3. Performance Evaluation and Related Discrepancies

More recently, it is observed that the research in the area of electrocatalytic water-splitting is obsessed with achieving lower overpotential values. With rapid development of H_2 technologies, this trend is justified, as the first indication of commercial feasibility of a non-noble electrocatalyst must be its performance. However, when reporting the performance, some standard protocols must be adopted, to avoid wrong comparisons or overstating the obtained data. In the past couple of years, there have been some excellent reviews addressing this concern and laying some fundamental protocols for electrocatalytic testing and reporting of data.[82,83] Unfortunately, few reports abide by these protocols and hence the scope of making wrong comparisons increases. Here, we enlist some of the most common errors encountered while reporting performance data for metal borides/borates. For a detailed understanding of these protocols, the readers are advised to follow the reviews by Kibsgaard and Chorkendorff[83] and Kundu and co-workers[82]

3.1. Mass Loading

Increasing the amount of catalyst improves the number of active sites and hence the observed performance. In the context of metal borides/borates, some of the reports, especially involving porous substrates (examples discussed later) use a catalyst loading ranging from 1 mg cm^{-2}[84] to excess of 10 mg cm^{-2},[85] which translates into much lower overpotentials (<200 mV for OER). However, such high catalyst loadings are not useful as they do not offer cost-effective solutions when upscaled. Commercial water electrolyzers employ catalyst loadings that are as low as 0.25 mg cm^{-2}[86] and hence the reported data must correspond to lower loading amounts, typically in the range of 0.1–0.5 mg cm^{-2}.

3.2. Water Oxidation Overpotential

The most widely used metric for comparing the performance of different water-splitting electrocatalysts is the overpotential to achieve 10 mA cm^{-2}. In case of HER, this metric works well and gives a good comparison of the state-of-the-art materials. However, being a multistep reaction, OER is often accompanied by oxidation of the catalytic species to produce intermediates, giving rise to a huge oxidation wave, spanning from a few μA cm^{-2} to tens of mA cm^{-2}.[75,87,88] In such cases, the metric of 10 mA cm^{-2} is used precariously, leading to overestimated performances. In case of metal borides/borates, ideally the oxidation wave is observed in the first (or first few) cycle(s) and subsides in the subsequent cycles. The overpotential value must be reported from the scan where the contribution from catalyst oxidation wave is minimal and actual OER begins. To validate that the observed current is a result of OER alone and does not have any other contributions (such as corrosion or capacitive currents), it becomes essential to measure the volume and analyze the concentration of product gases. This can be done by performing long-term electrolysis tests in cells that are similar to Hoffmann apparatus, making it easier to separate the two gases.[89,90] Additionally, the composition of used electrolyte must be analyzed to confirm absence of leached atoms from the catalyst surface or from the surface of counter Pt electrode. Unfortunately, these practices are not very common and seldom reported for metal borides/borates.

3.3. Intrinsic Activity

The geometric performance of an electrocatalyst is not a standard parameter as the number of active sites differs for each catalyst and is influenced by morphological properties as well as surface roughness. In such a case, the most practical method is to also report the intrinsic activity of an electrocatalyst. The most common methods to estimate intrinsic activity are by determining the ECSA normalized activity or by calculating the turn-over frequency (TOF), which quantifies the activity at each catalytic site. Though these practices are usually reported for metal borides/borates, care must be taken to estimate the lower and upper limits of TOF, as it is very difficult to precisely determine the actual sites taking part in the reaction.[83]

In view of the above points, it is a challenging task to compare the performance of different electrocatalysts reported for metal borides/borates in literature. Hence, in the following sections, we have included the overpotential/activity values for only those reports that have followed accurate protocols in their experimentation.

4. Strategies Adopted to Enhance the Performance of Metal Borides

The above sections discussed the fundamental reasons explaining the enhancement in electrocatalytic performance of various metal borides and some of the erroneous reporting practices found in literature. In following sections, different material engineering strategies adopted to further improve the electrochemical activity of metal borides are highlighted.

4.1. Using Substrates

The activity of a catalyst can be improved by supporting it on suitable conducting substrates of high surface area. The use of conducting support not only provides better conduction

pathways but also makes it easier to integrate the catalysts in industrial setup. Over the last few decades, the use of porous carbon[91] and carbon derivatives (graphene, graphene oxide (GO), reduced graphene oxide (rGO), carbon nanotubes (CNTs), graphitic carbon nitride (g-C_3N_4), etc.) have been popular choices as conducting supports for catalytic reactions.[92–95] Li et al.[96] synthesized Co–B incorporated in porous carbon (Co–B/C) using a metal organic framework (MOF) precursor, resulting in Co–B with a very high Brunauer–Emmett–Teller (BET) surface area of 119 m^2 g^{-1}. Owing to the high conductivity of carbon, a faster charge transfer was observed in Co–B/C and an overpotential to achieve 10 mA cm^{-2} (η_{10}) = 320 mV was required for catalyzing OER in 1 M KOH. Arivu et al.[97] synthesized Ni_3B-rGO composite and drop-casted it on carbon fiber paper for use as a free-standing anode. Similarly, cobalt borate (Co–B_i) nanosheets[32] were supported on graphene and showed a hierarchical structure of aggregated ultrathin nanosheets. An improvement in OER rate was observed in both cases. The use of graphene/rGO provides high surface area and instantaneous charge transfer route that helps in improving the reaction rate. This was confirmed by electrochemical impedance spectroscopy (EIS) data for CoB_i NS/G which showed a much lower R_{ct} (12.3 Ω) as compared to bare Co–B_i catalyst (R_{ct} = 35.7 Ω). Schuhmann and co-workers[98] synthesized Co–B nanoparticles and then used them as a substrate to grow N-doped CNTs by chemical vapor deposition. It was observed that most of the Co–B nanoparticles were located on the surface of CNTs while some were encapsulated inside the tube. The electrochemical performance of the composite was evaluated for OER, establishing η_{10} = 370 mV in 0.1 M KOH with a stability for 51 h. Carbon cloth was also explored by many researchers as an efficient conducting substrate to electrodeposit borates for electrolytic water-splitting.[56,57,61,80,99]

Other than carbon derivatives, the use of metal foils/plates and high surface area metal foams are also an attractive alternative to support catalyst particles. For water-splitting, the conducting metal foam provides higher surface area, good conductivity, and also convenient path for produced gases to escape (through the pores). Catalyst can be deposited on such conducting foams very conveniently and then can be employed as free-standing electrodes for water-splitting. Liang et al.[85] used Ni foam as a support material to grow Ni–B nanoparticles which showed significant improvement in electrocatalytic performance as it required η_{20} = 125 mV and η_{100} = 360 mV for HER and OER, respectively, in 1 M KOH. However, it must be noted that a catalyst loading of 12.3 mg cm^{-2} was used in this work, which is very high and hence cannot be justly compared to the standard reports. Similarly, Co–B was also deposited on Ni foam[100] and Ni foil[69] wherein formation of curved nanosheets with a thickness of a few nanometers was observed on surface of Co–B/Ni foam, while Co–B/Ni foil displayed a porous nodule-like structure with large number of internal spaces. When tested in 1 M KOH, Co–B/Ni foam showed η_{10} = 110 and 315 mV, for HER and OER, respectively. Wang and co-workers[52] deposited Co–W–B on Ni foam and calcined at different temperatures to obtain a layered morphology consisting of polycrystalline phases of $Co(OH)_2$, CoO, and Co_3O_4. Nocera and co-workers[101] tested Co–B_i on a larger scale by electrodepositing it on a porous Ni foam and fluorine-tin oxide (FTO) coated glass. Co–B_i/Ni foam achieved 100 mA cm^{-2} at η = 360 mV and could maintain it for long hours (≈90 h). Taking a cue from the work of Nocera and co-workers, Bai and co-workers[102] electrodeposited Co–B_i and Co–P_i catalysts on 3D graphene foam. Co–B_i/Graphene foam composite yields η_1 = 315 mV, which is lower compared to Co–B_i/FTO,[101] indicating the advantage of porous and conducting graphene foam. Bimetallic borides such as Fe–Ni–B[84] and Ni–Co–B[103] were also grown on Ni foam, which yielded nanosheet-like (**Figure 7**a) and nanocotton like (Figure 7b) morphologies respectively, facilitating water oxidation process. Sun and co-workers[104] used electrodeposition technique to synthesize Co–B_i nanosheets array on Ti mesh substrate. When tested for OER, Co–B_i/Ti showed η_{10} = 469 and 400 mV in 0.1 and 0.5 M KB_i, respectively. Similarly, Ni–B_i nanosheets array derived from $NiSe_2$ were also deposited on Ti mesh forming vertically grown nanosheet array (Figure 7c).[105]

Cu plate[29] and Cu foil[106] were also used to deposit Ni–B films for studying HER and OER respectively. As deposited film shows compact semiglobular nanoparticles with some nanovoids that were formed due to escaping H_2 gas during the deposition process (Figure 7d,e). $NiB_{0.54}$/Cu plate catalyst showed η_{10} = 45, 54, and 135 mV in 0.5 M H_2SO_4, 1 M PBS, and 1 M KOH, respectively for HER. Apparently, the authors recorded HER activity of $NiB_{0.54}$/Cu plate better than that of Pt in pH 7 and pH 14.

Looking at the trend of above reports, it is suggested that carbon and graphene-based materials are the most suitable substrates for enhancing the reaction rate of metal boride electrocatalysts. This is due to the rapid electron transfer channel provided by the carbon and graphene-based materials. Though use of metal foams is a good strategy, the amount of catalyst loading on such substrates must be optimized to draw a fair comparison with other substrates. Metal foams also present challenges in determining the real active surface area owing to their 3D porous networks, making it difficult to determine the true activity of electrocatalysts supported on them.

4.2. Controlling Morphology/Nanostructuring

In electrocatalysis, surface morphology and hence surface area plays an influential role in governing the electrochemical performance of the catalysts. Hence, it is essential to modify the conventional synthesis methods to obtain unique nanostructures that present preferred active sites and higher surface area. As discussed previously, OER proceeds via surface oxides while presence of metallic core helps in conduction of charges in a more efficient way. Thus, formation of a core-shell structure with metallic core and oxide shell is a promising strategy for OER catalysts. Ni_3N@NiB_i nanosheets[107] were synthesized using this strategy, where the outer thin layer (4–5 nm) of Ni_3N is converted to amorphous NiB_i, while the core remains intact, yielding a core-shell assembly (**Figure 8**a). This unique catalyst required η_{10} = 405 and 382 mV to catalyze OER in 0.1 M KBi and 0.5 M KB_i solutions, respectively, which are lower than that of Ni_3N/Ti catalyst (η_{10} = 540 mV in 0.1 M KB_i). Lu et al.[49] developed Co–B@CoO nanoarrays (Figure 8b,c) where the outer surface

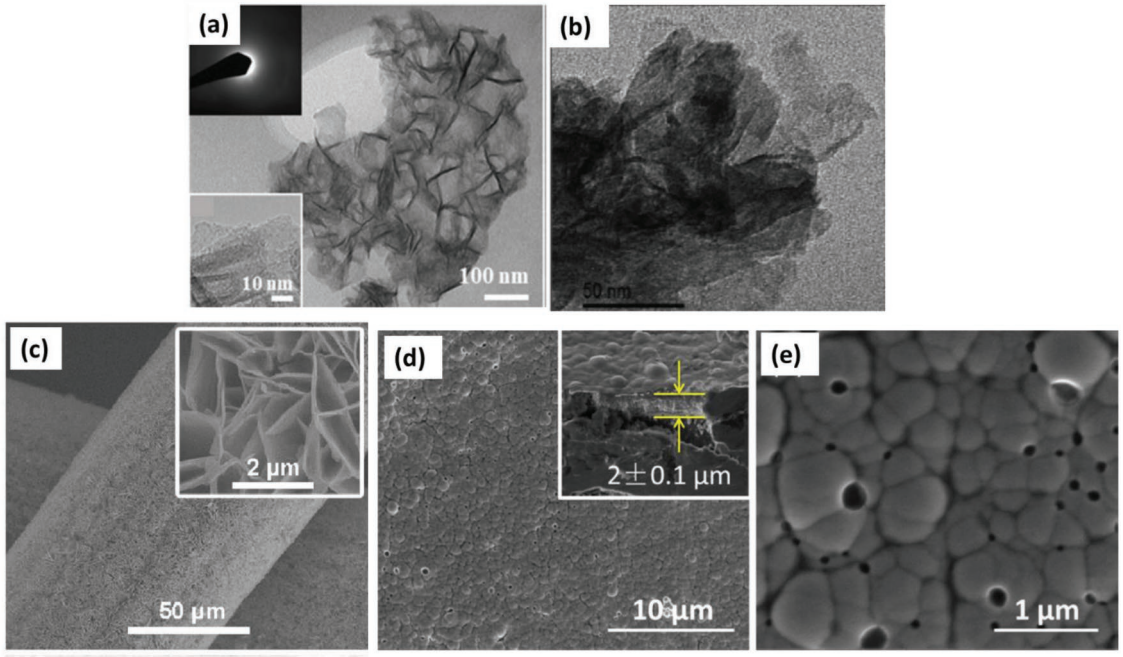

Figure 7. a) TEM image of Fe–Ni–B catalyst revealing the nanosheet-like morphology. Reproduced with permission.[84] Copyright 2018, Wiley-VCH. b) HR-TEM image of Ni–Co–B catalyst supported on Ni foam showing nanocotton-like morphology. Reproduced with permission.[103] Copyright 2019, Elsevier. c) SEM image of Ni–B_i nanoarrays supported on Ti mesh. Reproduced with permission.[105] Copyright 2017, Wiley-VCH. d) Low and e) high magnification SEM images of Ni–$B_{0.54}$ film deposited by electroless method (inset in (d) shows side-view SEM image of Ni–$B_{0.54}$ film). Reproduced with permission.[29] Copyright 2016, Elsevier.

(about 15–40 nm thick) is reduced to Co–B while the inner core of CoO remains intact, leading to improved electrochemical performance. In another work, Guo et al.[108] used $CoSe_2$/DETA (diethylenetriamine) nanosheets to support amorphous Co_2B for overall water-splitting in alkaline medium. TEM showed that small Co_2B nanosheets were uniformly grown on the surface of $CoSe_2$/DETA nanosheets. It was proposed that the rich amino groups (from diethylenetriamine) on the surface of $CoSe_2$ nanosheets created abundant nucleation sites for Co_2B growth. Xie et al.[31] synthesized Co@Co–B_i nanosheets supported on Ti mesh where the Co core exists in the form of nanoparticles whereas the shell of Co–B_i transforms into ultrathin nanosheets exposing more active sites. Yang et al.[109] employed a unique magnetic field assisted reduction method to obtain nanochains of Ni–Fe–B. As per the proposed mechanism (**Figure 9**), when $NaBH_4$ reduction initiates, the nanoparticles align linearly with the external magnetic field owing to the strong magnetic moment of metals and low boron content. As reduction proceeds, the content of B increases and the magnetic moment decays rapidly, forming a thick nonmagnetic amorphous layer of Ni–Fe–B. The optimized catalyst, i.e., 80Ni–20Fe–B nanochain (with Fe/Ni atomic ratio = 0.29) displayed OER mass activity of 64 A g^{-1} at an overpotential of 0.35 V in 0.1 M KOH, which was 7.6 times higher than the boron-free Ni/Fe nanochains.

Development of tailored nanostructures (such as core–shell presented above) not only presents higher number of surface-active sites but also charge conduction pathways that must be adopted to improve the performance of existing metal borides.

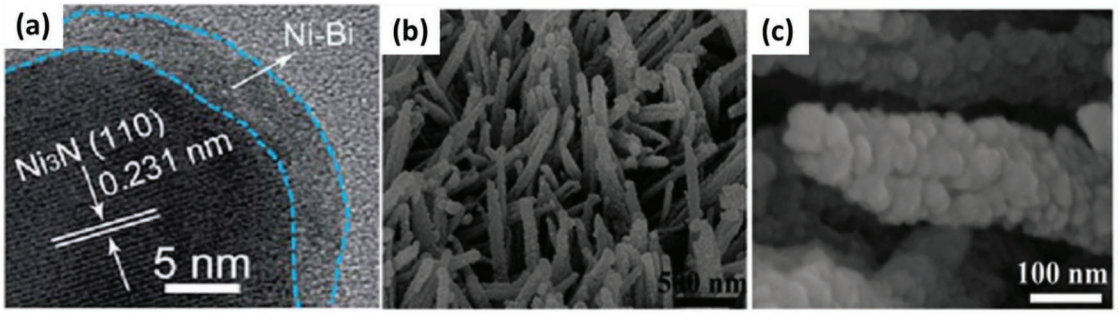

Figure 8. a) HR-TEM image of Ni_3N@Ni–B_i catalyst showing the metallic (Ni_3N) core surrounded by a thin shell of NiB_i. Reproduced with permission.[107] Copyright 2017, Royal Society of Chemistry. b) Low and c) high magnification SEM images of Co–B@CoO/Ti. Reproduced with permission.[49] Copyright 2017, Wiley-VCH.

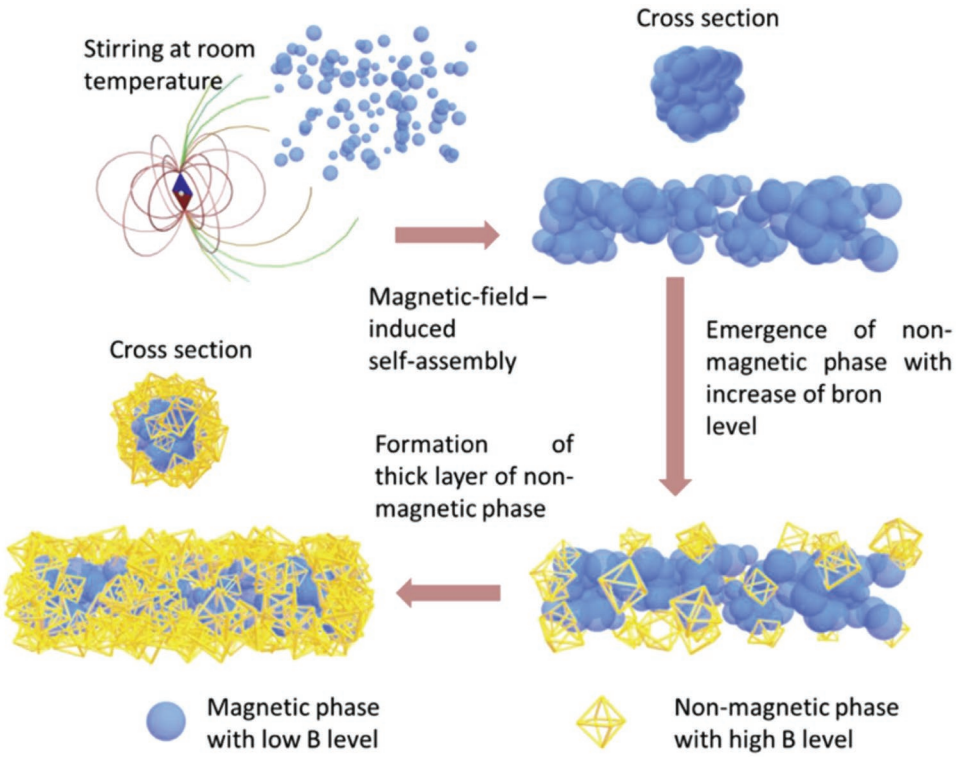

Figure 9. A schematic of the magnetic-field-induced self-assembly for synthesis of B-doped Fe/Ni nanochains. Reproduced with permission.[109] Copyright 2017, Elsevier.

4.3. Ternary Metal Incorporation

The success of binary metal borides instigated researchers to develop ternary borides for electrochemical water splitting. Borodzinski and Lasia[110] developed a series of metal (Rh, Ru, Cr, Co, Zn, Pt) doped Ni_2B catalysts for alkaline HER, by just introducing the desired dopant salt to the reaction solution. The amount of dopant elements was restricted to 0.5–10 wt% for Rh, Ru, Cr, and Co while 0.1–0.5 wt% for Pt. They found that introduction of Rh, Ru, Cr, and Co to Ni_2B resulted in improvement in HER activity but the performance remained same or even worsened by addition of Pt and Zn. The main reason for improvement in the performance of doped Ni_2B electrodes was attributed to their large surface area. In 2016, Patel and co-workers reported Co–Ni–B,[47] which showed no morphological or structural difference when compared to Co–B catalyst. The molar ratio of Ni/(Ni + Co) = 30% portrayed the best HER performance in neutral medium, higher than Co–B. Interestingly, this catalyst was tested in all pH medium, ranging from 1 to 14 and the HER performance increased with increasing pH. This manifested the suitability of Co–Ni–B in particular, and Co-based borides in general, for alkaline water electrolysis. The group of Zhang et al.[60] also synthesized Co–Ni–B and found that the molar ratio of Ni/(Ni + Co) = 10% yields the best performance for OER in 1 M KOH. Co–Ni–B supported on Ni foam,[51] carbon cloth[61] and rGO[111] were reported by different groups in a bid to lower down the overpotential. For HER, Co–Ni–B/CC[61] shows a lower overpotential of η_{10} = 80 mV (**Figure 10**a), which was also attributed to the formation of very small-sized particles with average diameter of 5–10 nm (Figure 10b).

Similar to the inclusion of Ni, the group of Patel and co-workers tried inclusion of Mo to develop Co–Mo–B[50] catalyst for overall water-splitting. Unlike Co–B and Co–Ni–B, as prepared Co–Mo–B catalyst showed polycrystalline nature (**Figure 11**a) consisting of Co–B and Co metal phases. Inclusion of Mo in Co–B (molar ratio of Mo/(Mo + Co) = 3%)

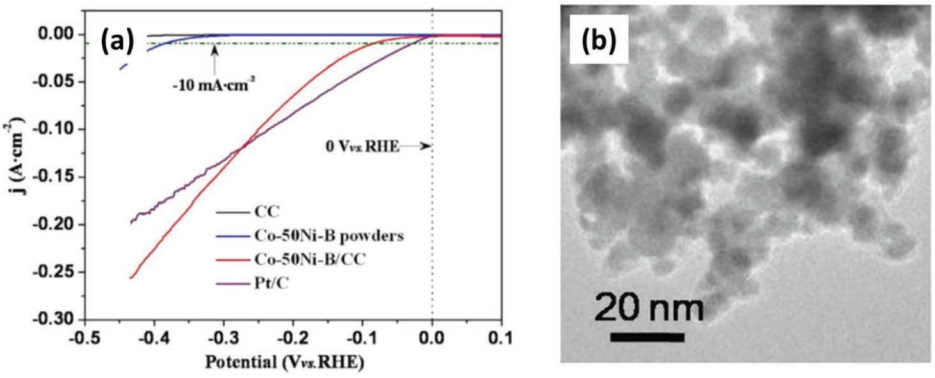

Figure 10. a) Cathodic polarization curves for Co–50Ni–B/CC, Co–50Ni–B, CC, and Pt/C in 1.0 M KOH. b) TEM image of Co–50Ni–B/CC catalyst. Reproduced with permission.[61] Copyright 2018, Elsevier.

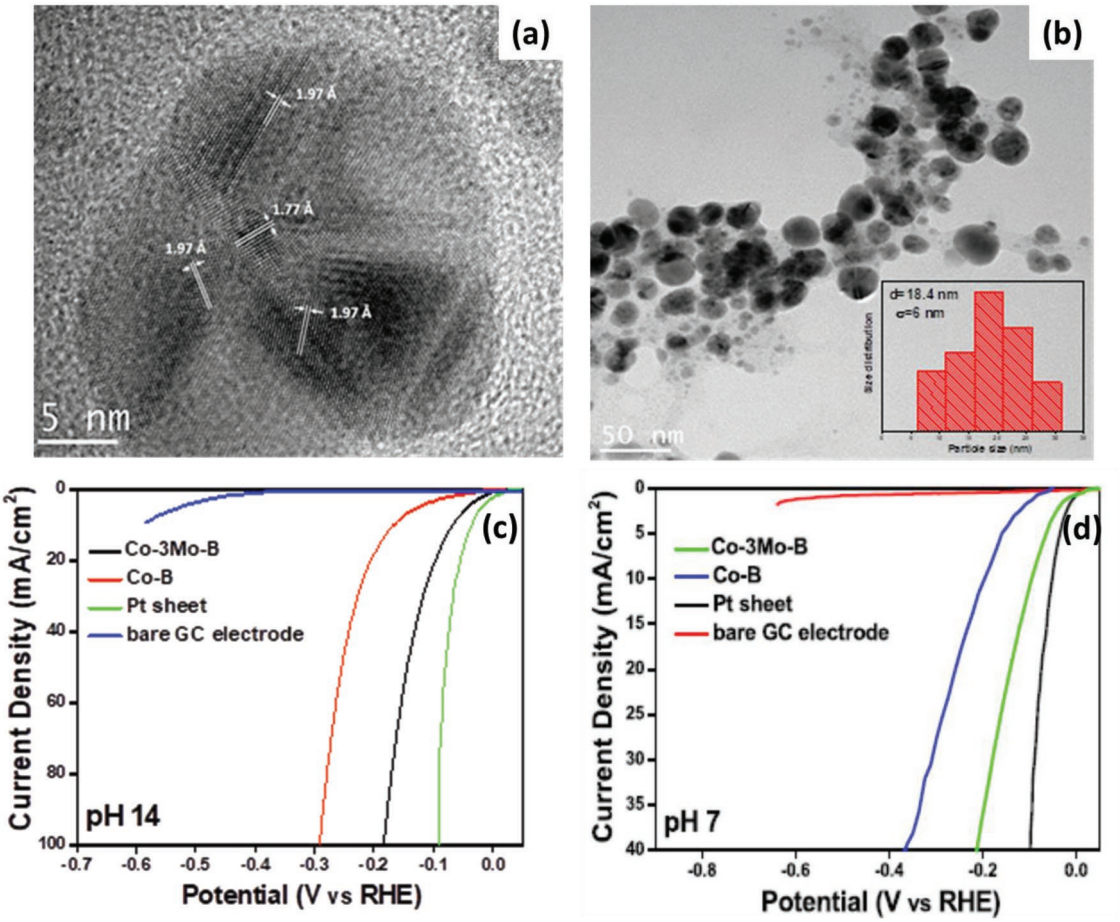

Figure 11. a) HR-TEM image of a representative Co–3Mo–B particle indicating formation of nanosized polycrystalline domains. b) TEM image and particle size distribution of Co–3Mo–B nanoparticles. Linear polarization curves for HER on Co–3Mo–B, Co–B, bare GC, and Pt in c) pH 14 and d) pH 7. Reproduced with permission.[50] Copyright 2017, Elsevier.

led to formation of smaller-sized nanoparticles (Figure 11b) with high surface area, which contributed toward its higher performance. Co–Mo–B showed excellent HER activity in alkaline and neutral medium, as it required just η_{10} = 66 mV (Figure 11c) and 96 mV (Figure 11d) in both media, respectively. The catalyst showed reasonably good performance for OER as well owing to the formation of CoOOH species on its surface, in alkaline medium. Some reports included Fe in Co–B to develop Co–Fe–B and Co–Fe–B–O as electrocatalytic materials by simple reduction process. Chen et al.[76] found that Co/Fe molar ratio of 2 (Co–2Fe–B) yields the most optimum performance for OER. The authors performed TOF calculations by considering the contributions of Co and Fe sites independently and speculated that the OER activity is dependent on both Co and Fe active sites. Liu et al.[74] optimized Fe/(Fe + Co) atomic ratio to 0.3 and developed amorphous Co–Fe–B–O catalyst with nanoparticles ranging from 20 to 50 nm. Co–Fe–B–O displayed improved OER activity owing to the formation of ultrathin nanosheets during water oxidation.

In 2015, Boettcher and co-workers[112] observed that oxidative conditioning of electrodeposited Ni–B_i films in potassium borate buffer led to an increment in the OER rate. XPS analysis of the films conditioned at an oxidative potential of 0.856 V (vs SCE) revealed presence of 14% Fe in the sample (**Figure 12**a). It was later found that the potassium borate used in the experiment had trace Fe impurities of ≈1 ppm, which was responsible for deposition of Fe on Ni–B_i films. This instigated the group to repeat the same OER tests in a pure Fe-free borate solution. In this case, post-conditioning XPS showed absence of Fe and the OER current was very low as compared to that containing Fe (Figure 12b). After optimization, it was found that Fe content of 14% in Ni–B_i films led to the highest OER activity. When compared to pure Ni–B_i films, Ni–Fe–B_i films showed substantially higher TOF values (≈0.3 s^{-1} for Ni–B_i; ≈1.4 s^{-1} for Ni–Fe–B_i) and lower Tafel slope (78 mV dec^{-1} for Ni–B_i; 46 mV dec^{-1} for Ni–Fe–B_i). Amorphous Ni–Fe–B was also synthesized by Liu et al.[113] which showed granular morphology with particle size ranging from 30 to 50 nm. XPS analysis indicated a positive shift in the binding energies of Ni and Fe, as compared to Ni–B and Fe–B, suggesting electron deficiency and higher valence states of Ni and Fe in Ni–Fe–B. The best OER performance was reported when the atomic ratio of Fe to (Ni + Fe) was 20. Recently, a composite of NiFeB nanosheets[114] was made with rGO and sintered in Ar atmosphere at 400 °C to obtain the final nanocrystalline Ni–Fe–B/rGO catalyst. In 2017, Sun and co-workers[80] developed a bimetallic borate in the form of

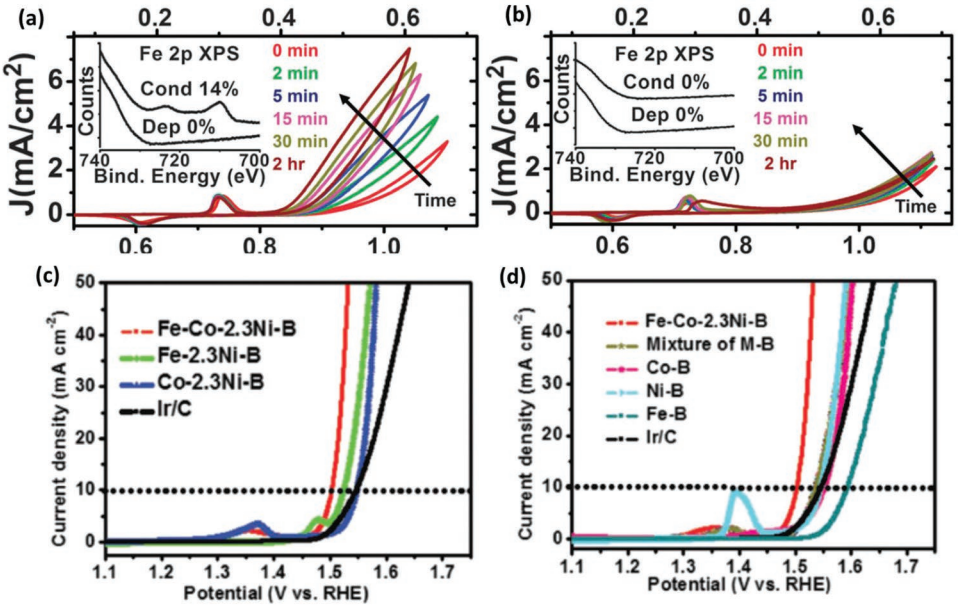

Figure 12. OER polarization curves and XPS data (inset) of Ni-(oxy)hydroxide–borate films in a) borate electrolyte with ≈1 ppm Fe contamination and b) Fe-free borate electrolyte. Reproduced with permission.[112] Copyright 2015, Royal Society of Chemistry. c,d) OER polarization curves for monometal, bimetal, and trimetal boron catalysts in 1 M KOH. Reproduced with permission.[75] Copyright 2018, Wiley-VCH.

Ni–Co–B_i, supported on carbon cloth for water oxidation in near neutral pH. Ni–Co–B_i/CC showed η_{10} = 388 and 316 mV in 0.1 and 0.5 M KB_i, respectively, indicating that this bimetallic borate has better catalytic performance than the binary borates (Co–B_i,[104] Ni–B_i[105]).

Thus, it turns out that ternary metal borides comprising of Co, Ni, Fe, and Mo yield better electrocatalytic performances than single metal borides. Inclusion of other earth-abundant elements such as Cu, Mn, Cr, etc. must also be tried to seek out the most suitable element configurations.

4.4. Quaternary Metal Incorporation

From above examples, the success of binary as well as ternary metal borides in catalyzing water-splitting reactions is clearly evident. Also, one can see that ternary borides are more efficient than their binary counterparts. In 2018, Wang and co-workers[75] synthesized a quaternary metal boride in the form of Fe–Co–Ni–B yielding completely amorphous spherical nanoparticles with average size of 30–40 nm. XPS analysis also indicated the usual trend of reverse electron transfer from B to metals. The optimized quaternary catalyst showed impressive OER rate (η_{10} = 274 mV) in 1 M KOH (Figure 12c,d). Recently, a quaternary alloy of vanadium doped cobalt nickel boride (VCNB) was developed in the form of hollow nanoprisms.[87] When the catalyst was supported on Ni foam, an overpotential of only 280 mV was required to achieve 30 mA cm^{-2} in 1 M KOH, demonstrating the combined advantages of metal incorporation, nanostructuring and porous metal foam. In this work, the authors reported a value of 30 mA cm^{-2} owing to the huge oxidation wave overlapping the current density of 10 mA cm^{-2}. However, just increasing the number of metal components does not always assist in improving the catalytic activity. Yang et al.[48] synthesized various binary and quaternary boron compounds with Co–Fe, Ni–Fe, Ba–Sr–Co–Fe, and La–Sr–Co–Fe. Among these, binary boron compounds exhibited higher OER mass activity than the quaternary ones. In case of quaternary compounds, inclusion of less active components (Ba, La, Sr) led to a reduction in the number of active components (Ni, Fe), causing a decline in the OER activity. This suggests that identification and incorporation of active elements in the formation of quaternary alloy is very important, in order to achieve new benchmarks in performance. However, at the same time, efforts are needed to understand the role of each participating element so as to understand the chemistry of such complex alloys.

4.5. Incorporation of Phosphorous (P)

Similar to incorporation of metals, P was included to form a ternary alloy of Co–P–B. Co–P–B/rGO[54] catalyst afforded η_{10} of 639 and 400 mV for HER and OER, respectively, in pH 7. Co–B–P was also deposited on Ni foam,[59] wherein an optimized B/P atomic ratio of 3 showed η_{10} = 42 mV for HER in 1 M KOH with a Tafel slope of 42.1 mV dec^{-1} (however with a loading of 5 mg cm^{-2}). The group of Sun and co-workers developed ternary P-incorporated borates[56,57] using a combination of synthesis techniques. Amorphous Co–P–B catalyst was also electrodeposited on carbon paper by Kim et al.[55] The competitive transfer of electrons from B to Co and Co to P creates a synergy that provides better HER rate in Co–P–B. This was a rare report showcasing the HER activity of Co based boride in acidic medium, as the instability of Co in acidic medium is well known. However, the authors did not report any stability measurements in the acidic solution to complement their performance results. Similar to P, inclusion of other metalloids can be made to obtain ternary borides. The inclusion of two

metalloids may present interesting avenues for fundamental research in the area of water electrolysis.

5. Synthesis Routes to Obtain Metal Borides

So far, we discussed the properties that are responsible for imparting electrochemical activity to different metal borides and various strategies that are used to enhance their activity. In this section, we look at the synthesis routes that have been employed to develop different metal borides/borates. Historically, the first synthesis of a metal boride was reported in early 19th century,[115] while the earliest report for water-splitting using transition-metal boride dates back to 1974, when Kuznetsova and co-workers[116] studied the reaction kinetics of hydrogen evolution on some metal borides. In 1981, Osaka et al.[117] investigated Co_xB, Ni_xB, Fe_xB, and LaB_6 for oxygen evolution in 6 M KOH. The metal powders were mixed with B powder, pressed and sintered in Ar atmosphere for different intervals. The authors used the same sintering method to develop bimetallic borides, i.e., Co–Fe–B, Co–Ni–B, and Co–Mn–B for OER.[118] Following these reports, the late 1980s saw a new interest in using commercially available amorphous borides for electrochemical water-splitting.[119–123] In 1986, Kreysa and Håkansson[119] tested a number of commercial glasses containing multiple metals (Fe, Ni, Co, Mo, Pd, Cu, Ti) and metalloids (B, P, Si) for cathodic and anodic reactions in 1 M KOH, at different temperatures, amongst which $Fe_6Co_{20}Si_{10}B_{10}$ was highly active for HER and OER while $Co_{50}Ni_{25}Si_{15}B_{10}$ was the most active for OER.[120] Schulz and co-workers[121] prepared amorphous $Ni_{0.65}Al_{0.1}B_{0.25}$ and $Ni_{0.70}Mo_{0.20}Si_{0.05}B_{0.05}$ alloys using melt-spinning technique and tested their cathodic performance in 30% KOH solution. Thorpe and co-workers[124] also synthesized amorphous composite borides such as $Co_{50}Ni_{25}Si_{15}B_{10}$, $Ni_{50}Co_{25}Si_{15}B_{10}$, and $Ni_{50}Co_{25}P_{15}B_{10}$ using melt-spinning technique for HER. The decade of 1990 saw few more reports on development of transition-metal borides for water-splitting.[110,125–127] However, rather than using commercial glasses or energy intensive techniques (such as melt-spinning), researchers started exploring simpler synthesis routes to manufacture boride electrocatalysts. Based on the literature reports after this decade, one can find that the synthesis of metal borides was mainly carried out using five different routes, namely, chemical reduction, electroless deposition, electrodeposition, solid-state heating, and chemical vapor deposition/boronization. The following section gives a brief detail of each of these techniques and their influence on the physical and/or chemical properties of the final metal borides.

5.1. Chemical Reduction

Chemical reduction of metal salts with a strong borohydride is one of the simplest techniques used to obtain pure metal borides. Using this method, borides of first-row transition metals namely, Fe, Co, and Ni can be readily formed. The general reduction reaction for any metal ion (M) can be represented by Equation (7)

$$4M^{2+} + BH_4^- + 8OH^- \rightarrow 4M + BO_2^- + 6H_2O \quad (7)$$

As an example, we see the reduction of cobalt chloride to form Co_2B,[128,129] in Equation (8) below

$$2CoCl_2 + 4NaBH_4 + 9H_2O \rightarrow Co_2B + 4NaCl + 12.5H_2 + 3B(OH)_3 \quad (8)$$

It can be seen from Equation (8) that excess of BH^{4-} ions reduces Co^{2+} to form binary boride (Co_2B) with some water-soluble by-products that can be separated out by filtration. In these reactions, the amount of borohydride is usually more than the metal precursor so that no metal ions are left unreacted.[129] The reaction is spontaneous and exothermic, resulting in large amounts of effervescence. Within a few minutes, the reaction is usually completed, resulting in black precipitates (commonly seen for most metal salts), which can be separated and dried. The borohydride salt plays a dual role of reducing agent as well as the boron source. Due to ease of availability and nontoxicity, sodium borohydride ($NaBH_4$)[130] has been the most prevalent reducing agent/boron source used in these types of reactions. It must be noted that this method of synthesis yields completely amorphous metal borides, which might be attributed to the spontaneity of the reduction process. In most cases, NaOH or KOH is added to borohydride solution to maintain an alkaline environment and control the rate of reaction.[130]

For water-splitting applications, one of the first reports of using chemical reduction method can be traced back to 1992, where Los and Lasia[125] prepared amorphous Ni_2B by reduction of nickel acetate with $NaBH_4$ and obtained higher HER rate compared to Ni powder. In 2015, Patel and co-workers[26] employed a similar synthesis approach to obtain amorphous Co–B catalysts (**Figure 13**a,b) and used them for water-splitting in neutral conditions. Since then, a number of reports[28,47,48,50,53,71,75,76,108] were made on development of Co borides using chemical reduction route. Masa et al.[28] prepared amorphous Co–B and annealed it under He at various temperatures. They observed that below 400 °C, the amorphous nature of Co–B is maintained but above that value it starts crystallizing to Co_2B phase (Figure 13c,d). In 2017, the same group synthesized Ni_xB[71] and similar to their Co_2B report, Ni_xB was also annealed at different temperatures of 300, 600, and 1000 °C. At 300 °C, the catalyst remained amorphous but with higher annealing temperatures, it crystallized into mixed phases of Ni_3B and Ni_2B. The authors found that the amorphous Ni_xB phase was electrochemically more active than the poly-crystalline phase. Employing reduction process, Li et al.[53] synthesized Fe-based boride (FeB_2) particles using $LiBH_4$ as a reducing agent and tetrahydrofuran (THF) as the reflux medium. Here, THF was used as the solvent to obtain boron-rich samples, which is difficult to control in aqueous medium. In the same work, Fe_2B particles were also synthesized in aqueous medium. Both the samples were annealed in N_2 gas at 600 °C to obtain pure crystalline phases. Wang and co-workers[131] performed chemical reduction in an ice bath, under Ar environment, and used different Co precursors (chloride, nitrate, acetate, sulfate) to control the morphology of the resultant Co–B catalyst. They observed that nitrate precursor suppressed the rapid reduction of Co ions, leading to formation of 2D nanosheets, while chloride precursor promoted fast reduction, leading to 3D nanoparticle formation.

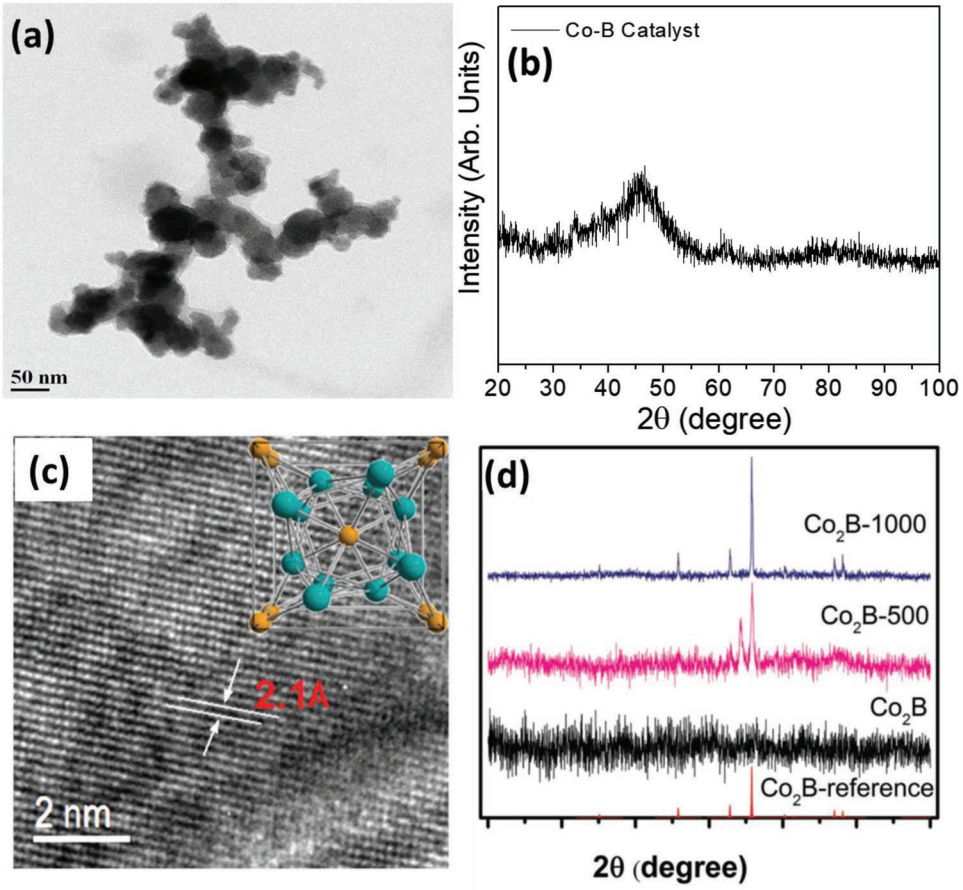

Figure 13. a) TEM image and b) XRD pattern of Co–B nanoparticles synthesized by chemical reduction method. Reproduced with permission.[26] Copyright 2015, Elsevier. c) HRTEM image of annealed Co_2B catalyst (Co_2B-500), inset: unit cell structure of Co_2B. d) XRD data showing the changes in crystallinity of Co_2B catalyst with increasing annealing temperature. Reproduced with permission.[28] Copyright 2016, Wiley-VCH.

5.2. Electroless Deposition

Though chemical reduction method discussed above is a very convenient synthesis technique, the nanopowder obtained is usually in an agglomerated form, thus possessing very low surface area. Also, for practical applications, the catalyst needs to be coated on particular substrates. In such cases, alternative synthesis methods such as electroless deposition, which employs reduction process to obtain coatings, seem more appropriate. Electroless deposition/plating was first introduced industrially by Brenner and Riddel in 1946.[132] Since then, there have been multiple modifications made to it, as per the required applications. Following the popularity of this technique in obtaining amorphous phosphides using hypophosphite as the reducing agent,[132] metal borides were also synthesized. For metal borides, the two main reducing agents being used for electroless depositions are dimethylamino borane (DMAB) and $NaBH_4$. However, $NaBH_4$ is a far stronger reducing agent as well as more cost-effective, when compared to DMAB.[133] Hence, majority of the present day electroless deposition procedures employ $NaBH_4$ as the reducing agent. A detailed study of the factors affecting the rate of electroless deposition in a Ni bath can be found in the report by Hwang and Lo[133] Using this method, the two most prevalent binary borides—Ni–B and Co–B were deposited by various groups for electrolytic water-splitting.[27,29,51,52,59,85,100,106] Amorphous Ni–B was grown directly on glassy carbon electrode by Zeng et al.[27] One of the main steps in electroless deposition is the activation of the substrate. In this report, glassy carbon (GC) was activated by applying an anodizing potential of 2.0 V versus Ag/AgCl in a phosphate buffer. Ni–B nanoparticles grown by this technique are amorphous with average size of 80 nm and depict a flower-like inner structure (**Figure 14**a,b). The catalyst (Ni–B) deposited by electroless method yields better performance when compared to the same catalyst prepared using conventional reduction method. This is ascribed to the flower-like morphology of the catalyst obtained with electroless deposition. It also demonstrates the advantage of electroless method over conventional reduction method to obtain nanostructured borides.

5.3. Electrodeposition

Electrodeposition is an age-old technique used industrially for a variety of materials. Prior to 1995, a lot of research was carried out on electrodeposition of Ni[134,135] under various conditions and studying their effect on its HER performance. Following

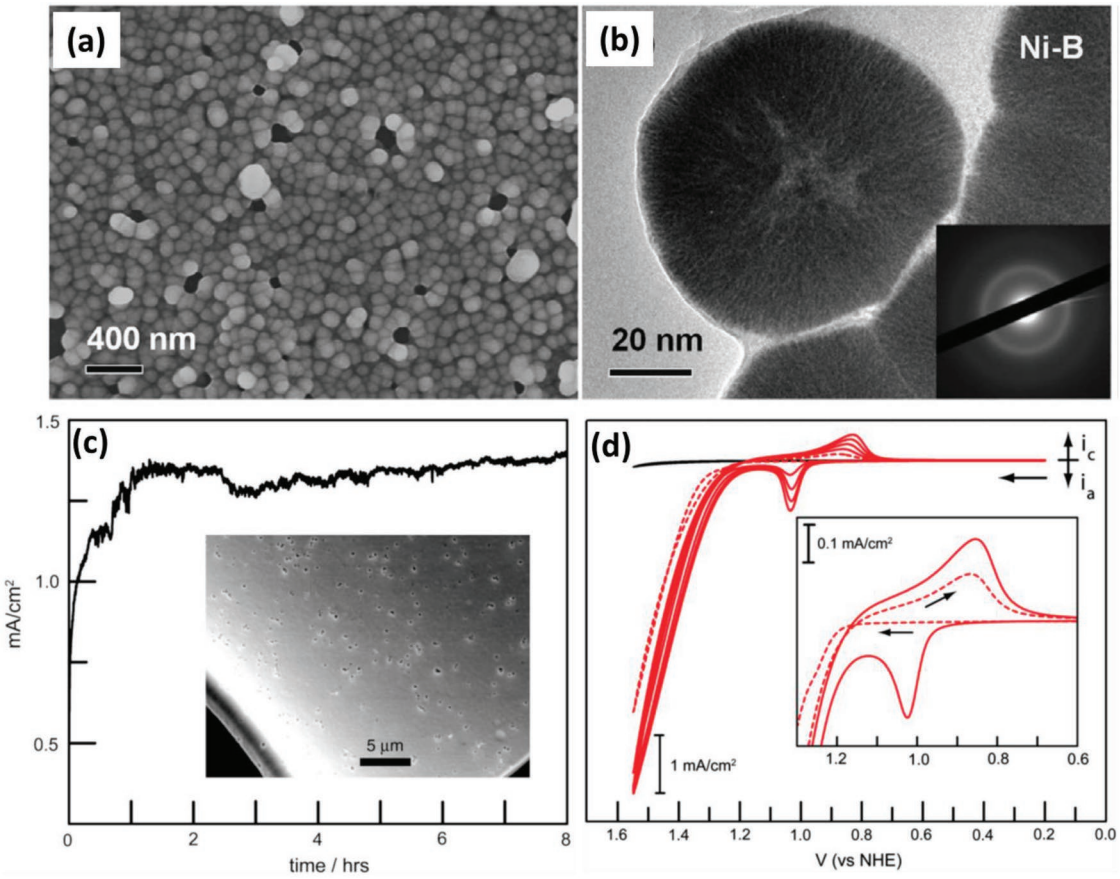

Figure 14. a) SEM image of electroless deposited Ni–B particles. b) TEM image of a single Ni–B particle depicting the flowerlike inner structure. Reproduced with permission.[27] Copyright 2016, Wiley-VCH. c) Variation in current density during bulk electrolysis using Co–B_i film in pH 9.2. Inset: SEM of Co–B_i film prepared by electrodeposition. d) Successive CV scans during electrodeposition, showing an increase of the anodic peak current for the redox event centered at ≈1.0 e. Inset: first (- - -) and second (—) CV scans. Reproduced with permission.[23] Copyright 2010, National Academy of Sciences.

his previous work on Ni electrodeposition, in 1994 Ndzebet and Savadogo[126] electrodeposited Ni–B on stainless steel in a bath containing H_3BO_3, $(NH_4)_2SO_4$, Na_2SO_4, and Ni_2B to study the HER performance. The seminal work of Nocera and Kanan in 2008[24] reported in situ deposition of Co phosphate (Co–P_i) on ITO in a pH 7 phosphate buffer and its OER performance in the same solution. This report fuelled the implementation of electrodeposition technique to obtain self-healing electrocatalysts in near neutral solutions. Following this, Nocera's group extended their work to develop different cobalt based oxygen evolution catalysts (Co-OEC)[22] by using different electrolyte solutions, namely, methyl phosphonate and borate buffer. The electrodeposited Co–B_i films were completely amorphous and showed spherical nodules that merge into larger aggregates upon full duration of electrolysis. With the successful demonstration of Co-OEC, the same group developed Ni–B_i films[23,35,72,136] electrodeposited on ITO coated glass (Figure 14c) from a borate electrolyte containing Ni^{2+} ions. While performing electrodeposition, the area under cathode and anode increased with successive scans, suggesting growth of catalyst (Figure 14d) in a layered manner, also providing a simple way to tune the thickness of the catalyst film.[23] Electrodeposition was used extensively by the group of Xuping Sun to develop various binary and ternary borates for water-splitting in various pH solutions.[56,57,80,99,104,105,107] However, it must be noted that the borate catalysts obtained by electrodeposition technique have majorly been restricted to OER tests in near-neutral solutions only.

5.4. Solid-State Methods

As seen in above sections, it is pretty easier to synthesize borides based on Co, Ni, Fe using their ionic salts. However, the same cannot be said about Mo-based borides, as synthesizing them in pure phase is a challenging task. Fokwa and co-workers[30] synthesized different Mo-based borides, namely, Mo_2B, α-Mo–B, β-Mo–B, and MoB_2 by arc melting process. In this process, Mo and B powders were mixed in desired ratios and pressed into pellets, followed by their arc-melting under Ar gas. All the desired phases were obtained with 90% purity and 10% contamination of Mo and other binary boride phases. The same group improved their work by successfully synthesizing a pure-phase sample in the form of Mo_2B_4, using tin flux method.[33] This was the first report of a pure phase Mo boride synthesized for electrocatalytic water-splitting. In this method, Mo and B powders were mixed with Sn and pressed into a pellet, followed by high temperature annealing and

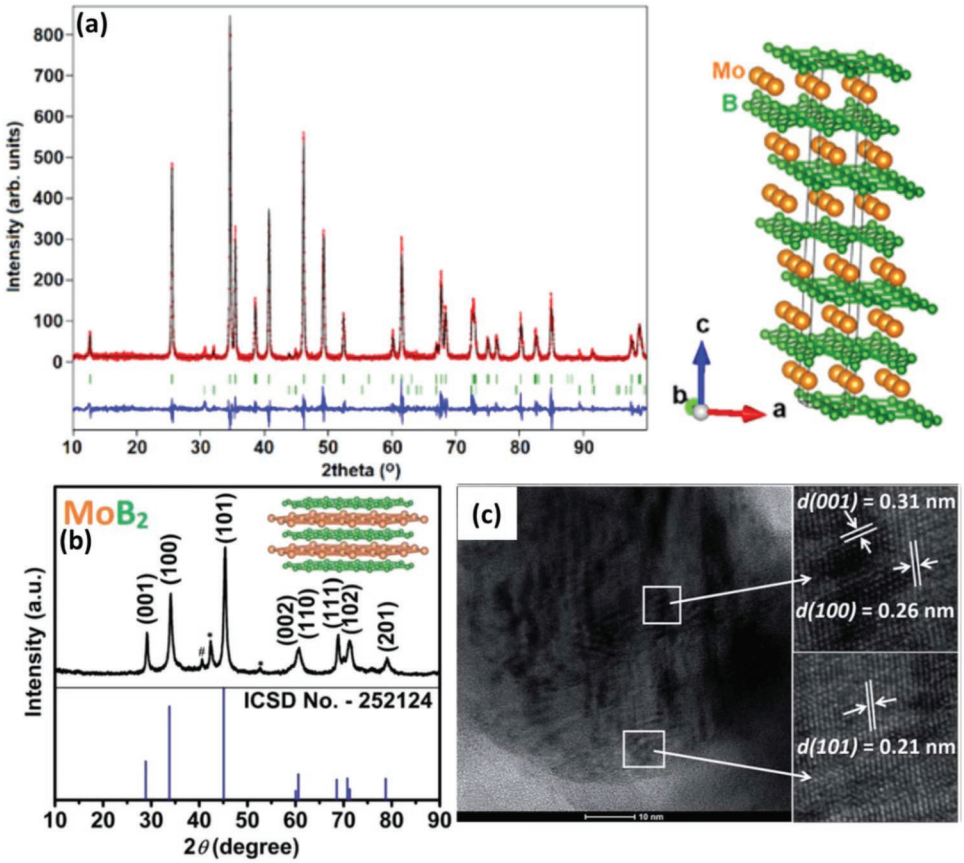

Figure 15. a) (Left) Rietveld refined XRD data for Mo_2B_4. (Right) Crystal structure of Mo_2B_4. Reproduced with permission.[33] Copyright 2017, American Chemical Society. b) XRD data of MoB_2 nanoparticles along with the reference pattern. The impurity peaks are indicated by #: Mo and *: β-MoB. Inset: layered crystal structure of MoB_2. c) HR-TEM image of MoB_2 nanoparticle showing presence of multiple lattice planes. Reproduced with permission.[34] Copyright 2017, Royal Society of Chemistry.

post-treatment with conc. HCl (to remove Sn). The method yielded pure-phase Mo_2B_4 powder (**Figure 15**a) with irregular shaped particles and a wide distribution of sizes ranging from 1 to 10 µm. To take advantage of the active MoB_2 phase, the same group used a single-step solid-state metathesis (SSM) process to obtain nanocrystalline MoB_2.[34] In this method, $MoCl_5$ and MgB_2 powders were mixed in desired ratios and pressed into pellets, followed by heating at 650 °C under Ar pressure and post-treatment with HCl (to remove $MgCl_2$). This method employs lower temperature and shorter synthesis duration when compared to arc-melting and tin flux methods used before. However, some impurities of Mo and β-Mo–B could not be eliminated in this method (Figure 15b). Unlike previous methods, this technique yielded nanosized particles ranging from 30 to 60 nm, displaying several lattice planes (Figure 15c). Schaak and co-workers[137] synthesized Mo–Al–B, belonging to a class of layered compounds (MAB), structurally analogous to MAX phases.[138] Mo–Al–B possess orthorhombic structure consisting of Mo–B layers alternately separated by two Al layers (**Figure 16**a). The interleaved Al layer is bonded by weak metallic bonding with the Mo–B layers and can easily be etched out chemically to obtain 2D Mo–B sheets. The synthesis of Mo–Al–B single crystals was performed by using Al flux method where Mo, B, and Al powders are mixed and annealed at high temperature, followed by digestion of Al flux by HCl. Mo–Al–B crystals were then treated with NaOH to etch Al from the interlayers, followed by soaking in urea solution to expand the interlayers (Figure 16b,d).

Employing another solid-state technique, i.e., ball-milling, Chen and co-workers[139] synthesized different phases of Co boride for water oxidation in alkaline media. By choosing the desired mole ratio of Co and B powders and adjusting the rotation speeds, three different phases of Co boride, specifically, Co–B, Co_2B, and Co_3B were obtained. Structurally, the obtained phases were completely pure, unlike Mo-borides where obtaining a single phase is difficult.

5.5. Chemical Vapor Deposition/Boronization

Wang et al.[140] used chemical vapor deposition to synthesize ultrathin Mo_3B films on Mo foil. The boron source (mixture of boron and boron oxide powder) was kept at one end and the target (Mo foil) was kept at the other end of a CVD furnace and heated to high temperatures. B_2O_2 vapor from the source is transported to Mo foil by high-purity H_2 gas, which also acts as reducing gas, to form Mo_3B ultrathin films. Liu et al.[141] used a solvothermal carbonization method to synthesize Co_2B/Co/N–B–C/B_4C hybrid catalyst which exhibited Co_2B as well as Co metallic phases immobilized on graphitic carbon

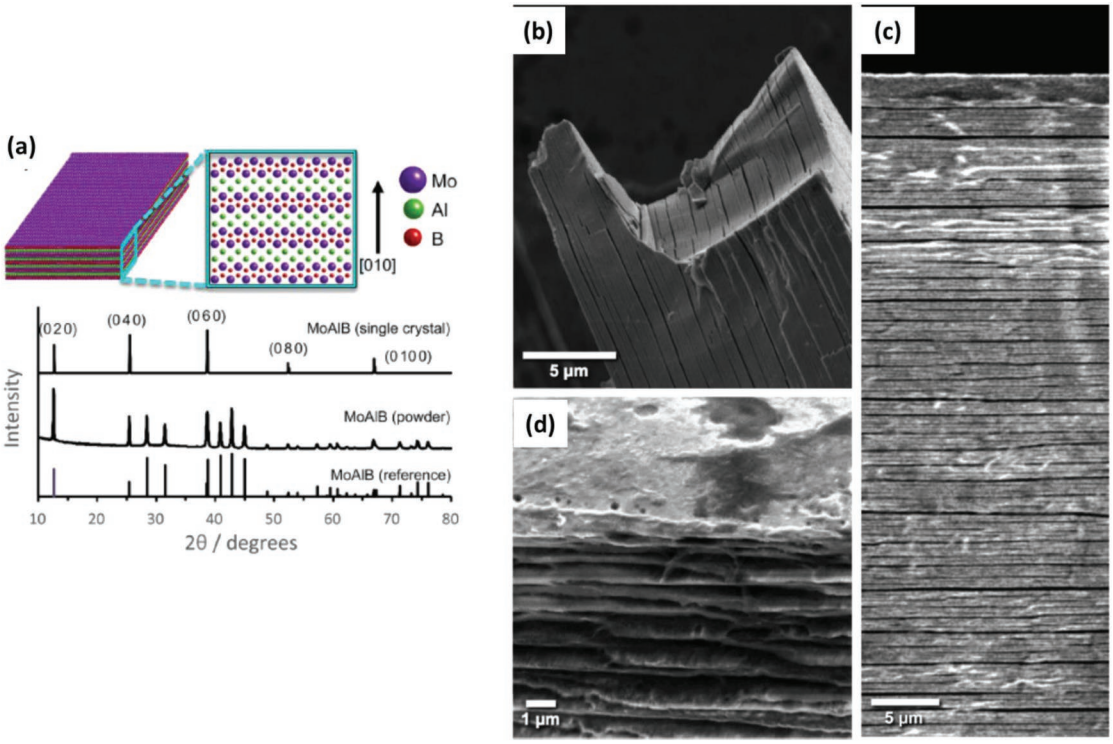

Figure 16. a) Schematic with crystal structure of MoAlB and the corresponding XRD patterns. SEM images of etched MoAlB single crystals after b) treatment with 10% NaOH, c) HER catalysis and fragmentation, and d) treatment with 10% NaOH followed by intercalation with 25% urea. Reproduced with permission.[137] Copyright 2017, American Chemical Society.

layers. Recently, a boronization strategy was developed to grow single phase metal boride layers on different metal substrates (Ni, Co, Fe, NiFe alloy, and SUS 304).[88] The synthesis method involved burying the metal substrate in boronizing agents (amorphous boron, potassium, fluoroborate), followed by thermal treatment in air at 800 °C. These boronized surfaces showed remarkable stability in 30% KOH solutions for OER, maintaining a current density in excess of 500 mA cm^{-2} for about 200 h.

After going through all the synthesis routes, it would be appropriate to suggest that chemical reduction method, to obtain nanopowders and coatings, is the most facile and economical technique to produce metal borides. Owing to its simplicity, it is also viable for plant-scale production. However, for development of pure-phase Mo-based borides, more research efforts are needed to search for less energy intensive techniques. The recently developed boronization technique is an impressive method to obtain stable catalyst surfaces, however more efforts are needed to tune it to achieve lower overpotentials.

At this point, the electrocatalytic capability of metal borides/borates is very well established. The section below gives a glimpse of the application of this family of electrocatalysts in a complementary strategy of photocatalytic water-splitting.

6. Metal Borides as Cocatalysts for Photocatalytic Water-Splitting

In photocatalytic water-splitting, different strategies are used to improve the efficiency of the photosensitive materials.[4,142] One of the many prominent strategies is the incorporation of an electrochemically active catalyst on the surface of the photosensitive material. The electrocatalysts thus incorporated (so called "cocatalysts") facilitate water-splitting mechanism in different ways, leading to an improvement in the overall efficiency of the system. An intensive review on cocatalysts for photocatalytic water-splitting is provided by Qiao and co-workers[143] Being electrochemically active, metal borides are promising candidates for use as cocatalysts, as reported by many authors. Cheng and co-workers[144] synthesized TaB_2/Ta_2O_5 core/shell heterostructure (**Figure 17**a) to serve as a visible light photocatalyst. Due to lattice mismatch between the two, Ta_2O_5 shows lattice distortion, which directly alters its electronic structure. This results in narrowing of the bandgap of Ta_2O_5 from 4.1 to 3.8 eV (Figure 17b), causing a little more absorption of UV-photons. The authors proposed a charge-separation mechanism where photogenerated electrons from Ta_2O_5 are transferred to TaB_2 (Figure 17c), which acts as the electron collector, thereby reducing recombination. Thus, incorporation of TaB_2 plays a dual role of narrowing the bandgap and separation of photogenerated charges, leading to an improvement in the photocatalytic efficiency. Yang and co-workers[145] developed a nanostructured composite of Ni–B/CdS and Ni–Co–B/CdS for photocatalytic hydrogen evolution. Ni–Co–B/CdS composite yielded an improvement in the photocatalytic efficiency by 36 times as compared to CdS alone, proving a vast improvement owing to the cocatalyst incorporation. Likewise, Ni–Co–B was also employed in a 3D photocathode comprising of Cu_2O, carbon film and graphene oxide (Cu_2O/C/NiCoB/GO) to improve the HER rate.[146] Sun and co-workers[147] loaded

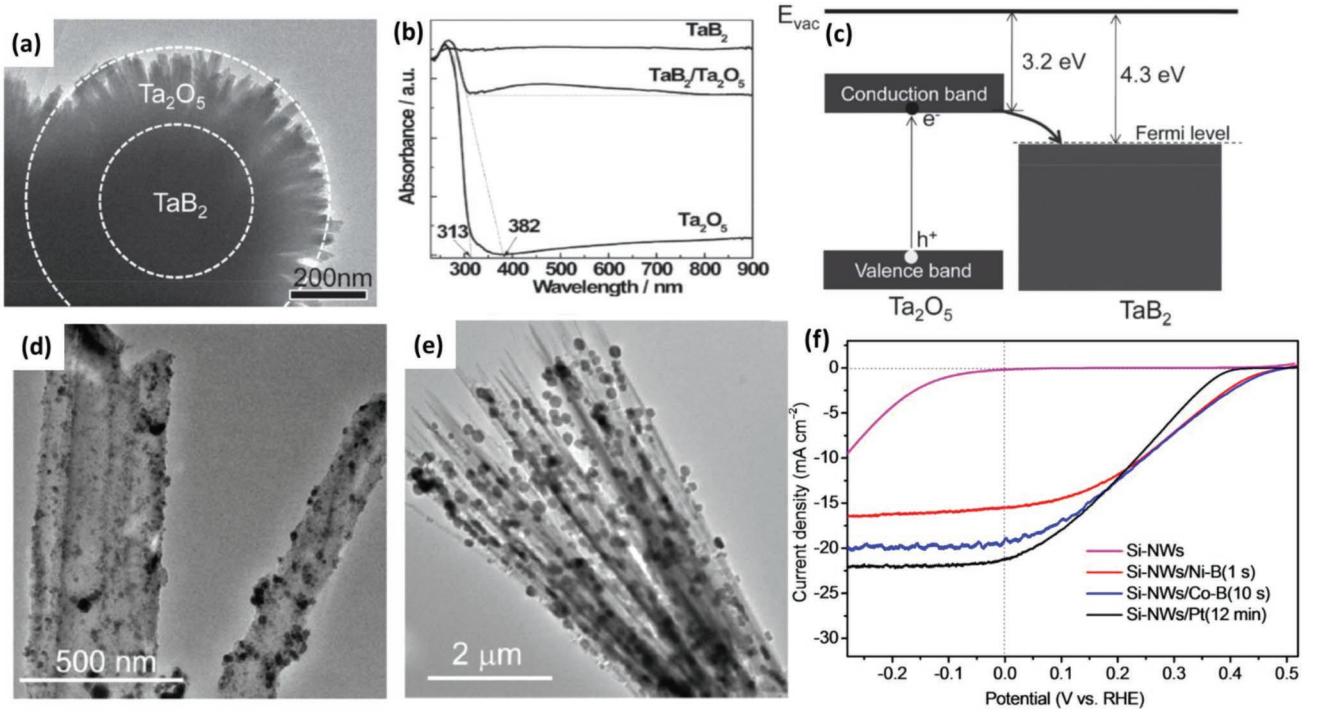

Figure 17. a) TEM image showing the core/shell structure of TaB_2/Ta_2O_5. b) UV–vis absorption spectra for TaB_2/Ta_2O_5, TaB_2 and Ta_2O_5 nanorods. c) Schematic showing the band edge alignments of Ta_2O_5 and TaB_2 with possible charge transfer pathway. Reproduced with permission.[144] Copyright 2014, Wiley-VCH. TEM images of d) Ni–B and e) Co–B decorated Si-NWs. f) Polarization curves of Si-NWs, Si-NWs/Ni–B, Si-NWs/Co–B, and Si-NWs/Pt photocathodes under 100 mW cm^{-2} illumination, in pH 7. Reproduced with permission.[147] Copyright 2016, American Chemical Society.

Ni–B and Co–B on Si nanowires (NWs) using electroless plating (Figure 17d,e) and used them as photocathodes for water reduction in neutral medium (Figure 17f). Interestingly, the authors reported half-cell photopower conversion efficiency of Ni–B/Si NWs (2.45) and Co–B/Si NWs (2.53) comparable to that of Pt/Si NWs (2.46), under similar test conditions. This suggests that Co–B and Ni–B can act as substitutes for Pt cocatalyst in neutral medium. Similarly, Ni–B was also loaded on $BiVO_4$[148] (**Figure 18**a) and g-C_3N_4[149] (Figure 18b) by different methods to improve their photocatalytic performance. Fe–B coated Fe_2O_3 nanorod photoanodes fabricated by Zou and co-workers[150] showed increment in photocurrent density (Figure 18c) and enhancement in incident photon-to-current conversion efficiency (IPCE) (Figure 18d) over the whole spectrum. Recently, Cheng and co-workers[151] reported TiB_2/TiO_2 core/shell particles were TiO_2 shell consists of mixed anatase and rutile phases. They observed a downward shift in the valence band edge of TiO_2, thereby increasing the oxidative capability and improving the efficiency. Thus, it can be seen that incorporation of metal borides as cocatalyst is a highly promising prospect, acting as substitutes for precious metal catalysts.

7. Conclusions and Perspectives

This paper provides an in-depth review of the emergence of metal borides as a promising family of electrocatalysts for water-splitting reactions. It sheds light on the reasons that give rise to electrochemical activity in various metal borides and borates. Though a unanimous theory governing the water-splitting mechanism in borides cannot be established, this review comprehensively compiles all the different proposed mechanisms. A comment is also made on the erroneous practices in data reporting within the literature. Looking at the different experimental strategies, one can conclude that incorporation of a second element as well as use of porous/carbon substrates are the best ways to improve the catalytic performance of base metal borides/borates. Tables 1 and 2 provide detailed expression of the electrochemical performance of all the metal borides and borates reported so far, for a comprehensive understanding of the readers. Based on this review, we intend to conclude whether it is worthy of carrying out further research in this family of electrocatalysts or not. To simplify this goal, we look at metal borides/borates from two perspectives—i) commercial viability and ii) fundamental understanding and challenges.

7.1. Commercial Viability

The commercial viability of metal borides/borates is assessed based on the following crucial parameters.

7.1.1. Performance

Figure 19 compares the OER performance of metal borides and borates with that of precious metal catalysts (RuO_2,[32] IrO_2[152]) as well as best representatives from other family of

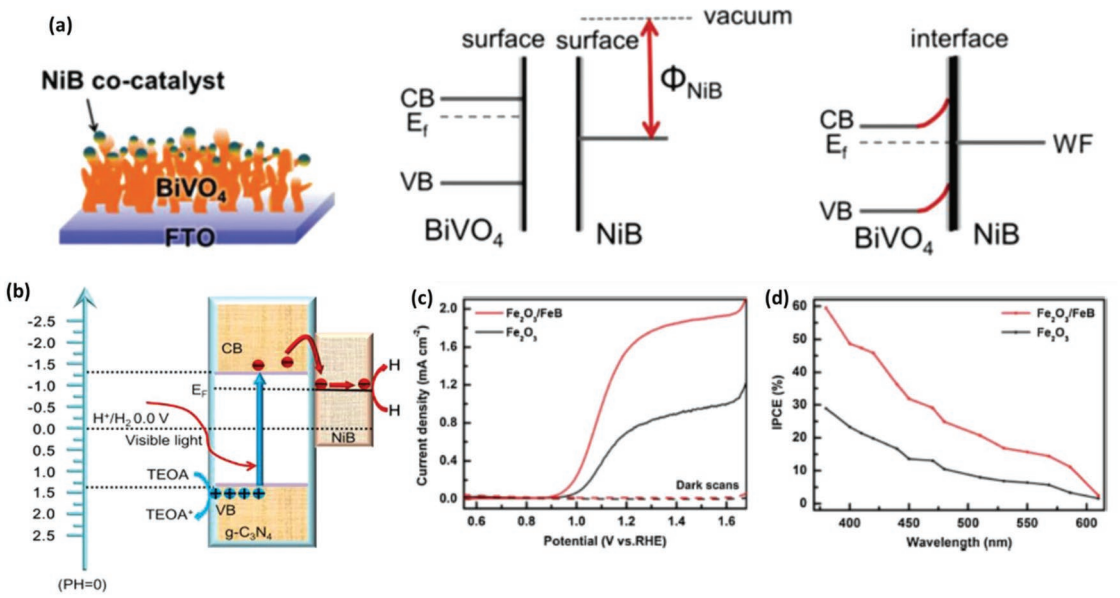

Figure 18. a) Schematic showing decoration of Ni–B nanoparticles over $BiVO_4$ and the proposed charge separation mechanism. Reproduced with permission.[148] Copyright 2017, Royal Society of Chemistry. b) Proposed charge separation and transfer mechanism in g-C_3N_4/$NiB_{7.5}$ photocatalyst, under light irradiation. Red and blue spheres denote photoinduced electrons and holes, respectively. Reproduced with permission.[149] Copyright 2018, American Chemical Society. c) Polarization curves and d) IPCE spectra measured at 1.23 V versus RHE for bare Fe_2O_3 and Fe_2O_3/Fe–B photoanodes. Reproduced with permission.[150] Copyright 2017, Elsevier.

nonprecious metal catalysts (phosphides,[64,65] carbides,[153,154] sulfides,[155] nitrides[156]). As the amount of catalyst governs the OER performance, we restrict to only those catalysts that use a loading < 3 mg cm^{-2}. Also, as majority of OER catalysts are reported in alkaline medium, the chart represents only these catalysts, except metal borates that are reported for near-neutral solution (pH 9.2). The chart also includes only those reports where accurate protocols were followed for data and performance representation. It can be seen that the overpotentials of in situ formed metal borates is on the higher side, with the lowest overpotential of 316 mV for $NiCoB_i$/CC catalyst, for a loading of 2.1 mg cm^{-2}.[80] On the other hand, metal borides show lower overpotential than even the precious metal electrocatalysts, with as low loading as 0.3 mg cm^{-2}. The OER performance of metal borides is also on par with other nonprecious metal electrocatalysts. It must be noted that Fe–Ni–B/NF[84] catalyst could achieve a low overpotential of 237 mV with a moderate loading of 1.0 mg cm^{-2}, which reiterates the superior OER performance of metal borides in alkaline medium.

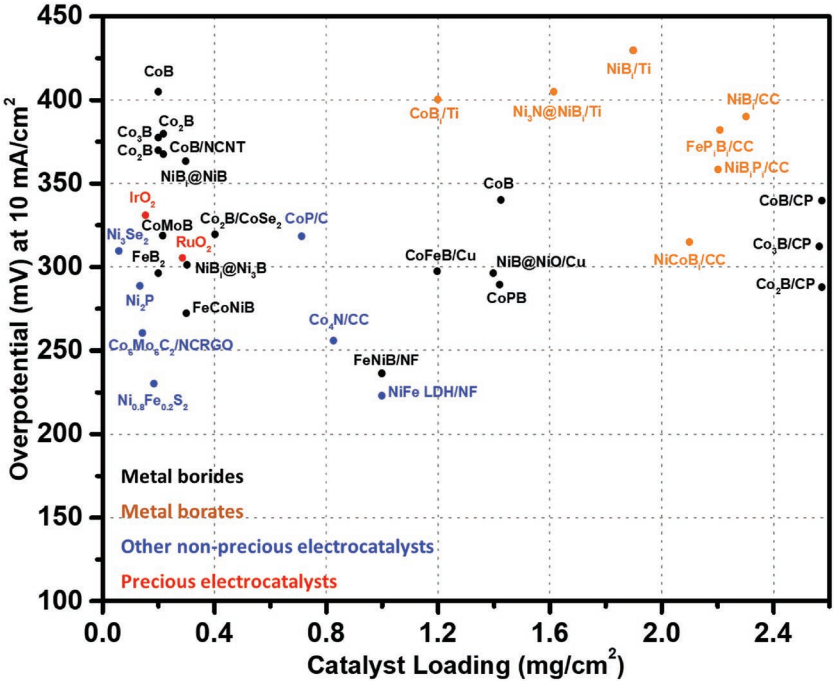

Figure 19. Comparison of OER performance for various metal boride/borate electrocatalysts reviewed in this article with respect to their mass loading. All catalysts are reported in pH 14 except metal borates that are reported in pH 9.2. The graph also indicates best catalysts from other families of nonprecious metal catalysts as well as precious metal-based catalysts. (Acronyms used—C: Vulcan carbon; CC: carbon cloth; CP: carbon paper; NF: Ni foam; Ni: Ni foil/plate; Ti: Ti mesh/foil.)

Figure 20 profiles metal borides along with some of the representative catalysts from other families of nonprecious metals and compare their HER performances with Pt. Here also, we restrict to only those electrocatalysts which reported a loading < 3 mg cm^{-2}. In acidic medium, very few metal borides are reported stable, but Ni boride catalysts seem to be as good as metal phosphides and carbides. In neutral medium, not many nonprecious metal catalysts work well, but metal borides show good stability and performance, approaching

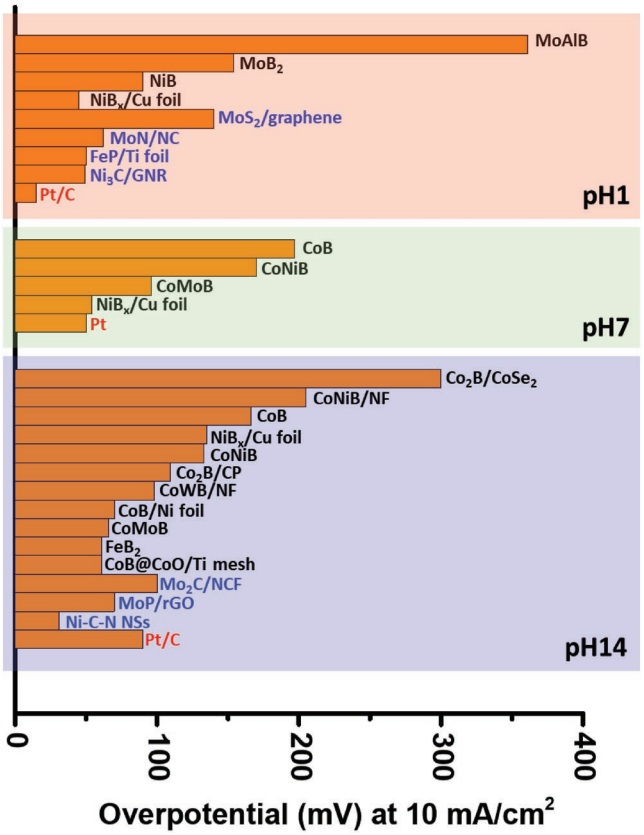

Figure 20. Comparison of HER performance for various metal boride electrocatalysts in different pH solutions with Pt as well as other nonprecious metal catalysts. (Acronyms used—C: Vulcan carbon; NC: N-doped carbon; GNR: graphene nanoribbons; CP: carbon paper; NF: Ni foam; Ni: Ni foil/plate; Ti: Ti mesh/foil; NCF: nanoparticles dispersed on carbon microflowers, NSs: nanosheets.)

that of Pt. In alkaline medium, metal borides work the best, many of them outclassing Pt catalyst. Overpotentials as low as 45,[29] 54,[29] and 61 mV[53] have been achieved by metal borides in acidic, basic, and alkaline media, respectively, approaching close to the thermoneutral voltage for H_2 evolution.

7.1.2. Stability

For OER, there has been no report on using metal borides in acidic medium, which reflects the instability of this family in acids. Even for HER, very few metal borides (Ni and Mo based) are stable in acidic solutions. However, metal borides show immense stability in neutral and alkaline solutions for HER as well as for OER.

7.1.3. Cost-Effectiveness and Earth-Abundance

Boron is relatively much cheaper and earth-abundant when compared to precious elements like Pt, Ru, Ir, and Pd. Most of the reported metal borides use transition metals, which are also low-cost and earth-abundant, thereby providing inexpensive alternatives to the conventional noble metals.

7.1.4. Ease of Synthesis

As elaborately discussed in this review, synthesis of metal borides can be carried out by facile methods such as chemical reduction, which can also be modified to produce coatings on desired substrates (electroless deposition). These methods can easily be upscaled for producing large size electrodes. Metal borates are synthesized using electrodeposition technique, which is also a well-established commercial route. The synthesis methods for metal borides/borates are less energy intensive and nontoxic when compared to those needed for synthesis of other nonprecious electrocatalysts (metal phosphides and sulfides), making them more preferable.

Based on the above assessment, we observe that the performance of metal borides has improved in leaps and bounds over the past few years. They also score highly for other requisite parameters listed above. For this reason, there is a realistic perspective that they can be used to replace the precious-metal catalysts, especially in alkaline water electrolyzers. With the development of neutral and near-neutral pH electrolyzers, metal borides/borates can be ideal electrode materials, as not many catalysts are active and/or stable in this regime. We suggest that the future work in metal borides/borates must focus on performing additional tests in extreme conditions (≈30 bar, 80 °C, >200 h stability), which will establish their reliability for industrial alkaline water electrolyzers.[7]

7.2. Fundamental Understanding and Challenges

From the point of view of fundamental understanding, a lot many aspects regarding the family of metal borides/borates are still not very clear. In case of amorphous metal borides, the most widely accepted reaction mechanism is based on the model that metal atoms (Co and Ni) act as the active center while boron donates electrons to enrich their d-band, preventing the metals against oxidation. This model of "reverse electron transfer" is experimentally confirmed and proved by computational simulations. However, the definitive reason for this reverse electron transfer in amorphous metal borides deserves to be further studied. In case of OER, it is known that boron does not act as the active center and assists the formation of active metal oxide/hydroxide species. However, the precise role of boron and the mechanism of this "assistance" is not understood. Being a low atomic number element, boron poses technical difficulties in its detection by common lab techniques. Though it can be studied using sophisticated methods like X-ray photoelectron spectroscopy or electron energy loss spectroscopy, conventional experiments may not be sufficient to reveal the true role of boron in metal borides. We suggest incisive experiments based on in situ/operando methods that can observe the variation in chemical behavior of boron before, during and after water-splitting tests. From this review, one can observe an improvement in the catalytic rates for ternary and quaternary metal borides, when compared to monometal borides. However, it is not known how the interaction between the base metal and boron is altered with addition of a second or third metal. The addition of a second metalloid (like P) in a metal boride

system also changes the reaction mechanism completely. The present literature does comment on the change of active catalytic centers in such systems, but no direct evidence exists. As suggested above, in-situ/operando tests coupled with computational tools must be employed to understand the role of foreign elements. Introduction of other nonmetals such as S, C, and N can also be tried to develop cross-breed electrocatalysts and study their fundamental properties and electrochemical behavior.

Some reports suggest that completely crystalline phases of metal borides are less active than their amorphous or partially crystalline counterparts, but it is not seen in all cases. For metal borides that are completely crystalline, identification of active center becomes an easier task, with DFT tools. In spite of this success, no efforts are taken to tailor the metal borides with an approach to expose more active planes, as commonly done with other catalysts (like MoS_2). We suggest targeted research to fabricate metal boride nanostructures with more exposed active sites. This will certainly lead to a huge leap in improving the performance of crystalline metal borides. In terms of stability, metal borides are not much stable in acidic medium, posing an issue for their use in proton exchange membrane (PEM) water electrolyzers, but Mo based borides are exception to this family that show good stability in acidic medium. However, synthesis of pure phase Mo borides is a difficult exercise, which needs to be addressed by more intensive efforts. New synthesis strategies must be adopted to develop Mo-based borides, not only in crystalline form but also in amorphous phase. The success of this will be a key to develop acid-stable metal borides, providing a major breakthrough. In the end, this review conveys a strong message that metal borides are an important piece of the jig saw puzzle that will complete the hunt for inexpensive electrocatalysts. They have great potential and are very likely to be incorporated in commercial alkaline water electrolyzers, if streamlined research will be performed for the next few years.

Acknowledgements

S.G. acknowledges the research grant from UK Commonwealth Commission through Commonwealth Rutherford Fellowship (INRF-2017-139). N.P. acknowledges UGC and SERB-DST for providing financial support through Faculty recharge program and Extra Mural project (FILE NO. EMR/2016/003028). M.K.P. acknowledges the seed funding obtained from EPSRC-GCRF No. 141131/155337.

Conflict of Interest

The authors declare no conflict of interest.

Keywords

earth-abundant metals, hydrogen evolution reaction, metal borates, metal borides, oxygen evolution reaction, water-splitting

Received: August 7, 2019
Revised: September 18, 2019
Published online: October 30, 2019

[1] Y. Hayakawa, S. Kambara, M. El-Shafie, *J. Power Energy Eng.* **2019**, *7*, 720.
[2] J. M. Ogden, *Fuel Future* **2002**, *55*, 69.
[3] T. J. Jacobsson, *Energy Environ. Sci.* **2018**, *11*, 1977.
[4] R. Shwetharani, M. Sakar, C. A. N. Fernando, V. Binas, R. G. Balakrishna, *Catal. Sci. Technol.* **2019**, *9*, 12.
[5] Z. Chen, T. F. Jaramillo, T. G. Deutsch, A. Kleiman-Shwarsctein, A. J. Forman, N. Gaillard, R. Garland, K. Takanabe, C. Heske, M. Sunkara, *J. Mater. Res.* **2010**, *25*, 3.
[6] P. C. K. Vesborg, B. Seger, I. B. Chorkendorff, *J. Phys. Chem. Lett.* **2015**, *6*, 951.
[7] M. Schalenbach, A. R. Zeradjanin, O. Kasian, S. Cherevko, K. J. J. Mayrhofer, *Int. J. Electrochem. Sci.* **2018**, *13*, 1173.
[8] S. Chen, S. S. Thind, A. Chen, *Electrochem. Commun.* **2016**, *63*, 10.
[9] M. Carmo, D. L. Fritz, J. Mergel, D. Stolten, *Int. J. Hydrogen Energy* **2013**, *38*, 4901.
[10] O. Schmidt, A. Gambhir, I. Staffell, A. Hawkes, J. Nelson, S. Few, *Int. J. Hydrogen Energy* **2017**, *42*, 30470.
[11] M. Schalenbach, G. Tjarks, M. Carmo, W. Lueke, M. Mueller, D. Stolten, *J. Electrochem. Soc.* **2016**, *163*, F3197.
[12] M. Zeng, Y. Li, *J. Mater. Chem. A* **2015**, *3*, 14942.
[13] N.-T. Suen, S.-F. Hung, Q. Quan, N. Zhang, Y.-J. Xu, H. M. Chen, *Chem. Soc. Rev.* **2017**, *46*, 337.
[14] F. Wang, T. A. Shifa, X. Zhan, Y. Huang, K. Liu, Z. Cheng, C. Jiang, J. He, *Nanoscale* **2015**, *7*, 19764.
[15] P. Xiao, W. Chen, X. Wang, *Adv. Energy Mater.* **2015**, *5*, 1500985.
[16] P. Yu, F. Wang, T. A. Shifa, X. Zhan, X. Lou, F. Xia, J. He, *Nano Energy* **2019**, *58*, 244.
[17] M.-I. Jamesh, X. Sun, *J. Power Sources* **2018**, *400*, 31.
[18] J. S. Kim, B. Kim, H. Kim, K. Kang, *Adv. Energy Mater.* **2018**, *8*, 1702774.
[19] R. D. L. Smith, M. S. Prévot, R. D. Fagan, S. Trudel, C. P. Berlinguette, *J. Am. Chem. Soc.* **2013**, *135*, 11580.
[20] S. Anantharaj, K. Karthick, S. Kundu, *Mater. Today Energy* **2017**, *6*, 1.
[21] M. E. G. Lyons, R. L. Doyle, M. P. Browne, I. J. Godwin, A. A. S. Rovetta, *Curr. Opin. Electrochem.* **2017**, *1*, 40.
[22] Y. Surendranath, M. Dinca, D. G. Nocera, *J. Am. Chem. Soc.* **2009**, *131*, 2615.
[23] M. Dincă, Y. Surendranath, D. G. Nocera, *Proc. Natl. Acad. Sci. USA* **2010**, *107*, 10337.
[24] M. W. Kanan, D. G. Nocera, *Science* **2008**, *321*, 1072.
[25] H. Vrubel, X. Hu, *Angew. Chem., Int. Ed.* **2012**, *51*, 12703.
[26] S. Gupta, N. Patel, A. Miotello, D. C. Kothari, *J. Power Sources* **2015**, *279*, 620.
[27] M. Zeng, H. Wang, C. Zhao, J. Wei, K. Qi, W. Wang, X. Bai, *ChemCatChem* **2016**, *8*, 708.
[28] J. Masa, P. Weide, D. Peeters, I. Sinev, W. Xia, Z. Sun, C. Somsen, M. Muhler, W. Schuhmann, *Adv. Energy Mater.* **2016**, *6*, 1502313.
[29] P. Zhang, M. Wang, Y. Yang, T. Yao, H. Han, L. Sun, *Nano Energy* **2016**, *19*, 98.
[30] H. Park, A. Encinas, J. P. Scheifers, Y. Zhang, B. P. T. Fokwa, *Angew. Chem., Int. Ed.* **2017**, *56*, 5575.
[31] C. Xie, Y. Wang, D. Yan, L. Tao, S. Wang, *Nanoscale* **2017**, *9*, 16059.
[32] P. Chen, K. Xu, T. Zhou, Y. Tong, J. Wu, H. Cheng, X. Lu, H. Ding, C. Wu, Y. Xie, *Angew. Chem., Int. Ed.* **2016**, *55*, 2488.
[33] H. Park, Y. Zhang, J. P. Scheifers, P. R. Jothi, A. Encinas, B. P. T. Fokwa, *J. Am. Chem. Soc.* **2017**, *139*, 12915.
[34] P. R. Jothi, Y. Zhang, J. P. Scheifers, H. Park, B. P. T. Fokwa, *Sustainable Energy Fuels* **2017**, *1*, 1928.
[35] C. L. Farrow, D. K. Bediako, Y. Surendranath, D. G. Nocera, S. J. L. Billinge, *J. Am. Chem. Soc.* **2013**, *135*, 6403.
[36] M. Yoshida, T. Iida, T. Mineo, T. Yomogida, K. Nitta, K. Kato, H. Nitani, H. Abe, T. Uruga, H. Kondoh, *Electrochemistry* **2014**, *82*, 355.

[37] Y. Jiao, Y. Zheng, M. Jaroniec, S. Z. Qiao, *Chem. Soc. Rev.* **2015**, *44*, 2060.
[38] M. R. G. de Chialvo, A. C. Chialvo, *J. Electroanal. Chem.* **1996**, *415*, 97.
[39] M. R. G. de Chialvo, A. C. Chialvo, *J. Braz. Chem. Soc.* **1994**, *5*, 137.
[40] P. Sabatier, *Ber. Dtsch. Chem. Ges.* **1911**, *44*, 1984.
[41] S. Trasatti, *J. Electroanal. Chem. Interfacial Electrochem.* **1972**, *39*, 163.
[42] M. M. Jaksic, *J. New Mater. Electrochem. Syst.* **2000**, *3*, 153.
[43] T. F. Jaramillo, K. P. Jørgensen, J. Bonde, J. H. Nielsen, S. Horch, I. Chorkendorff, *Science* **2007**, *317*, 100.
[44] P. Lazar, M. Otyepka, *Chem. - Eur. J.* **2017**, *23*, 4863.
[45] P. Liu, J. A. Rodriguez, T. Asakura, J. Gomes, K. Nakamura, *J. Phys. Chem. B* **2005**, *109*, 4575.
[46] L. C. Pauling, *Proc. R. Soc. London, Ser. A* **1949**, *196*, 343.
[47] S. Gupta, N. Patel, R. Fernandes, R. Kadrekar, A. Dashora, A. K. Yadav, D. Bhattacharyya, S. N. Jha, A. Miotello, D. C. Kothari, *Appl. Catal., B* **2016**, *192*, 126.
[48] Y. Yang, L. Zhuang, T. E. Rufford, S. Wang, Z. Zhu, *RSC Adv.* **2017**, *7*, 32923.
[49] W. Lu, T. Liu, L. Xie, C. Tang, D. Liu, S. Hao, F. Qu, G. Du, Y. Ma, A. M. Asiri, *Small* **2017**, *13*, 1700805.
[50] S. Gupta, N. Patel, R. Fernandes, S. Hanchate, A. Miotello, D. C. Kothari, *Electrochim. Acta* **2017**, *232*, 64.
[51] N. Xu, G. Cao, Z. Chen, Q. Kang, H. Dai, P. Wang, *J. Mater. Chem. A* **2017**, *5*, 12379.
[52] G. Cao, N. Xu, Z. Chen, Q. Kang, H. Dai, P. Wang, *ChemistrySelect* **2017**, *2*, 6187.
[53] H. Li, P. Wen, Q. Li, C. Dun, J. Xing, C. Lu, S. Adhikari, L. Jiang, D. L. Carroll, S. M. Geyer, *Adv. Energy Mater.* **2017**, *7*, 1700513.
[54] P. Li, Z. Jin, D. Xiao, *J. Mater. Chem. A* **2014**, *2*, 18420.
[55] J. Kim, H. Kim, S.-K. Kim, S. H. Ahn, *J. Mater. Chem. A* **2018**, *6*, 6282.
[56] M. Ma, D. Liu, S. Hao, R. Kong, G. Du, A. M. Asiri, Y. Yao, X. Sun, *Inorg. Chem. Front.* **2017**, *4*, 840.
[57] W. Wang, D. Liu, S. Hao, F. Qu, Y. Ma, G. Du, A. M. Asiri, Y. Yao, X. Sun, *Inorg. Chem.* **2017**, *56*, 3131.
[58] A. Chunduri, S. Gupta, O. Bapat, A. Bhide, R. Fernandes, M. K. Patel, V. Bambole, A. Miotello, N. Patel, *Appl. Catal., B* **2019**, *259*, 118051.
[59] H. Sun, X. Xu, Z. Yan, X. Chen, L. Jiao, F. Cheng, J. Chen, *J. Mater. Chem. A* **2018**, *6*, 22062.
[60] J. Zhang, X. Li, Y. Liu, Z. Zeng, X. Cheng, Y. Wang, W. Tu, M. Pan, *Nanoscale* **2018**, *10*, 11997.
[61] M. Sheng, Q. Wu, Y. Wang, F. Liao, Q. Zhou, J. Hou, W. Weng, *Electrochem. Commun.* **2018**, *93*, 104.
[62] Y. Matsumoto, E. Sato, *Mater. Chem. Phys.* **1986**, *14*, 397.
[63] W. T. Hong, M. Risch, K. A. Stoerzinger, A. Grimaud, J. Suntivich, Y. Shao-Horn, *Energy Environ. Sci.* **2015**, *8*, 1404.
[64] L.-A. Stern, L. Feng, F. Song, X. Hu, *Energy Environ. Sci.* **2015**, *8*, 2347.
[65] J. Chang, Y. Xiao, M. Xiao, J. Ge, C. Liu, W. Xing, *ACS Catal.* **2015**, *5*, 6874.
[66] X. Zhang, C. Si, X. Guo, R. Kong, F. Qu, *J. Mater. Chem. A* **2017**, *5*, 17211.
[67] D. Liu, Q. Lu, Y. Luo, X. Sun, A. M. Asiri, *Nanoscale* **2015**, *7*, 15122.
[68] B. R. Wygant, K. Kawashima, C. B. Mullins, *ACS Energy Lett.* **2018**, *3*, 2956.
[69] W. Hao, R. Wu, R. Zhang, Y. Ha, Z. Chen, L. Wang, Y. Yang, X. Ma, D. Sun, F. Fang, *Adv. Energy Mater.* **2018**, *8*, 1801372.
[70] C. Xue, G. Li, J. Wang, Y. Wang, L. Li, *Electrochim. Acta* **2018**, *280*, 1.
[71] J. Masa, I. Sinev, H. Mistry, E. Ventosa, M. de la Mata, J. Arbiol, M. Muhler, B. Roldan Cuenya, W. Schuhmann, *Adv. Energy Mater.* **2017**, *7*, 1700381.
[72] D. K. Bediako, B. Lassalle-Kaiser, Y. Surendranath, J. Yano, V. K. Yachandra, D. G. Nocera, *J. Am. Chem. Soc.* **2012**, *134*, 6801.
[73] M. Yoshida, Y. Mitsutomi, T. Mineo, M. Nagasaka, H. Yuzawa, N. Kosugi, H. Kondoh, *J. Phys. Chem. C* **2015**, *119*, 19279.
[74] G. Liu, D. He, R. Yao, Y. Zhao, M. Wang, N. Li, J. Li, *Int. J. Hydrogen Energy* **2018**, *43*, 6138.
[75] J. M. V. Nsanzimana, Y. Peng, Y. Y. Xu, L. Thia, C. Wang, B. Y. Xia, X. Wang, *Adv. Energy Mater.* **2018**, *8*, 1701475.
[76] H. Chen, S. Ouyang, M. Zhao, Y. Li, J. Ye, *ACS Appl. Mater. Interfaces* **2017**, *9*, 40333.
[77] J. Masa, C. Andronescu, H. Antoni, I. Sinev, S. Seisel, K. Elumeeva, S. Barwe, S. Marti-Sanchez, J. Arbiol, B. Roldan Cuenya, *ChemElectroChem* **2019**, *6*, 235.
[78] S. Gupta, H. Jadhav, S. Sinha, A. Miotello, M. K. Patel, A. Sarkar, N. Patel, *ACS Sustainable Chem. Eng.* **2019**, *7*, 16651.
[79] W.-J. Jiang, S. Niu, T. Tang, Q.-H. Zhang, X.-Z. Liu, Y. Zhang, Y.-Y. Chen, J.-H. Li, L. Gu, L.-J. Wan, J.-S. Hu, *Angew. Chem., Int. Ed.* **2017**, *56*, 6572.
[80] M. Ma, F. Qu, X. Ji, D. Liu, S. Hao, G. Du, A. M. Asiri, Y. Yao, L. Chen, X. Sun, *Small* **2017**, *13*, 1700394.
[81] J. Masa, W. Schuhmann, *ChemCatChem* **2019**, *11*, 1.
[82] S. Anantharaj, S. R. Ede, K. Karthick, S. S. Sankar, K. Sangeetha, P. E. Karthik, S. Kundu, *Energy Environ. Sci.* **2018**, *11*, 744.
[83] J. Kibsgaard, I. Chorkendorff, *Nat. Energy* **2019**, *4*, 430.
[84] J. M. V. Nsanzimana, V. Reddu, Y. Peng, Z. Huang, C. Wang, X. Wang, *Chem. - Eur. J.* **2018**, *24*, 18502.
[85] Y. Liang, X. Sun, A. M. Asiri, Y. He, *Nanotechnology* **2016**, *27*, 12LT01.
[86] K. A. Lewinski, D. van der Vliet, S. M. Luopa, *ECS Trans.* **2015**, *69*, 893.
[87] H. Han, Y.-R. Hong, J. Woo, S. Mhin, K. M. Kim, J. Kwon, H. Choi, Y.-C. Chung, T. Song, *Adv. Energy Mater.* **2019**, *9*, 1803799.
[88] F. Guo, Y. Wu, H. Chen, Y. Liu, L. Yang, X. Ai, X. Zou, *Energy Environ. Sci.* **2019**, *12*, 684.
[89] K. Fujii, T. Karasawa, K. Ohkawa, *Jpn. J. Appl. Phys.* **2005**, *44*, L543.
[90] M. S. Wrighton, D. S. Ginley, P. T. Wolczanski, A. B. Ellis, D. L. Morse, A. Linz, *Proc. Natl. Acad. Sci. USA* **1975**, *72*, 1518.
[91] F. Rodriguez-Reinoso, *Carbon* **1998**, *36*, 159.
[92] D. Haag, H. H. Kung, *Top. Catal.* **2014**, *57*, 762.
[93] D. Vairavapandian, P. Vichchulada, M. D. Lay, *Anal. Chim. Acta* **2008**, *626*, 119.
[94] S. Cao, J. Low, J. Yu, M. Jaroniec, *Adv. Mater.* **2015**, *27*, 2150.
[95] M. Cao, X. Zhang, J. Qin, R. Liu, *ACS Sustainable Chem. Eng.* **2018**, *6*, 16198.
[96] Y. Li, H. Xu, H. Huang, L. Gao, Y. Zhao, T. Ma, *Electrochem. Commun.* **2018**, *86*, 140.
[97] M. Arivu, J. Masud, S. Umapathi, M. Nath, *Electrochem. Commun.* **2018**, *86*, 121.
[98] K. Elumeeva, J. Masa, D. Medina, E. Ventosa, S. Seisel, Y. U. Kayran, A. Genç, T. Bobrowski, P. Weide, J. Arbiol, M. Muhler, W. Schuhmann, *J. Mater. Chem. A* **2017**, *5*, 21122.
[99] X. Ji, L. Cui, D. Liu, S. Hao, J. Liu, F. Qu, Y. Ma, G. Du, A. M. Asiri, X. Sun, *Chem. Commun.* **2017**, *53*, 3070.
[100] Z. Chen, Q. Kang, G. Cao, N. Xu, H. Dai, P. Wang, *Int. J. Hydrogen Energy* **2018**, *43*, 6076.
[101] A. J. Esswein, Y. Surendranath, S. Y. Reece, D. G. Nocera, *Energy Environ. Sci.* **2011**, *4*, 499.
[102] M. Zeng, H. Wang, C. Zhao, J. Wei, W. Wang, X. Bai, *Sci. Bull.* **2015**, *60*, 1426.
[103] S. Wang, P. He, Z. Xie, L. Jia, M. He, X. Zhang, F. Dong, H. Liu, Y. Zhang, C. Li, *Electrochim. Acta* **2019**, *296*, 644.
[104] L. Yang, D. Liu, S. Hao, R. Kong, A. M. Asiri, C. Zhang, X. Sun, *J. Mater. Chem. A* **2017**, *5*, 7305.
[105] R. Ge, X. Ren, F. Qu, D. Liu, M. Ma, S. Hao, G. Du, A. M. Asiri, L. Chen, X. Sun, *Chem. - Eur. J.* **2017**, *23*, 6959.

[106] J. Jiang, M. Wang, W. Yan, X. Liu, J. Liu, J. Yang, L. Sun, *Nano Energy* **2017**, *38*, 175.
[107] L. Xie, F. Qu, Z. Liu, X. Ren, S. Hao, R. Ge, G. Du, A. M. Asiri, X. Sun, L. Chen, *J. Mater. Chem. A* **2017**, *5*, 7806.
[108] Y. Guo, Z. Yao, C. Shang, E. Wang, *ACS Appl. Mater. Interfaces* **2017**, *9*, 39312.
[109] Y. Yang, L. Zhuang, R. Lin, M. Li, X. Xu, T. E. Rufford, Z. Zhu, *J. Power Sources* **2017**, *349*, 68.
[110] J. J. Borodzinski, A. Lasia, *J. Appl. Electrochem.* **1994**, *24*, 1267.
[111] J. Sun, W. Zhang, S. Wang, Y. Ren, Q. Liu, Y. Sun, L. Tang, J. Guo, X. Zhang, *J. Alloys Compd.* **2019**, *776*, 511.
[112] A. M. Smith, L. Trotochaud, M. S. Burke, S. W. Boettcher, *Chem. Commun.* **2015**, *51*, 5261.
[113] G. Liu, D. He, R. Yao, Y. Zhao, J. Li, *Nano Res.* **2018**, *11*, 1664.
[114] L. An, Y. Sun, Y. Zong, Q. Liu, J. Guo, X. Zhang, *J. Solid State Chem.* **2018**, *265*, 135.
[115] S. Carenco, D. Portehault, C. Boissiere, N. Mezailles, C. Sanchez, *Chem. Rev.* **2013**, *113*, 7981.
[116] V. A. Lavrenko, L. N. Yagupol'skaya, L. I. Kuznetsova, *Ehlektrokhimiya* **1974**, *10*, 1078.
[117] T. Osaka, H. Ishibashi, T. Endo, T. Yoshida, *Electrochim. Acta* **1981**, *26*, 339.
[118] T. Osaka, Y. Iwase, H. Kitayama, T. Ichino, *Bull. Chem. Soc. Jpn.* **1983**, *56*, 2106.
[119] G. Kreysa, B. Håkansson, *J. Electroanal. Chem. Interfacial Electrochem.* **1986**, *201*, 61.
[120] H. Alemu, K. Jüttner, *Electrochim. Acta* **1988**, *33*, 1101.
[121] J.-Y. Huor, M. Trudeau, L. Brossard, R. Schulz, *Int. J. Hydrogen Energy* **1989**, *14*, 319.
[122] H. Kronberger, C. Fabjan, G. Frithum, *Int. J. Hydrogen Energy* **1991**, *16*, 219.
[123] L. Vračar, B. E. Conway, *Int. J. Hydrogen Energy* **1990**, *15*, 701.
[124] K. Lian, D. W. Kirk, S. J. Thorpe, *Electrochim. Acta* **1991**, *36*, 537.
[125] P. Los, A. Lasia, *J. Electroanal. Chem.* **1992**, *333*, 115.
[126] E. Ndzebet, O. Savadogo, *Int. J. Hydrogen Energy* **1994**, *19*, 687.
[127] B. Mahdavi, D. Miousse, J. Fournier, H. Menard, J. Lessard, *Can. J. Chem.* **1996**, *74*, 380.
[128] G. N. Glavee, K. J. Klabunde, C. M. Sorensen, G. C. Hadjapanayis, *Langmuir* **1992**, *8*, 771.
[129] G. N. Glavee, K. J. Klabunde, C. M. Sorensen, G. C. Hadjipanayis, *Langmuir* **1993**, *9*, 162.
[130] H. I. Schlesinger, H. C. Brown, A. E. Finholt, J. R. Gilbreath, H. R. Hoekstra, E. K. Hyde, *J. Am. Chem. Soc.* **1953**, *75*, 215.
[131] J. M. V. Nsanzimana, L. Gong, R. Dangol, V. Reddu, V. Jose, B. Y. Xia, Q. Yan, J. Lee, X. Wang, *Adv. Energy Mater.* **2019**, *9*, 1901503.
[132] K. Krishnaveni, T. S. N. S. Narayanan, S. K. Seshadri, *Surf. Coat. Technol.* **2005**, *190*, 115.
[133] Y. L. Lo, B. J. Hwang, *Ind. Eng. Chem. Res.* **1994**, *33*, 56.
[134] O. Savadogo, S. Levesque, *J. Appl. Electrochem.* **1991**, *21*, 457.
[135] E. Ndzebet, O. Savadogo, *Int. J. Hydrogen Energy* **1992**, *17*, 751.
[136] D. K. Bediako, Y. Surendranath, D. G. Nocera, *J. Am. Chem. Soc.* **2013**, *135*, 3662.
[137] L. T. Alameda, C. F. Holder, J. L. Fenton, R. E. Schaak, *Chem. Mater.* **2017**, *29*, 8953.
[138] M. Naguib, M. Kurtoglu, V. Presser, J. Lu, J. Niu, M. Heon, L. Hultman, Y. Gogotsi, M. W. Barsoum, *Adv. Mater.* **2011**, *23*, 4248.
[139] X. Ma, J. Wen, S. Zhang, H. Yuan, K. Li, F. Yan, X. Zhang, Y. Chen, *ACS Sustainable Chem. Eng.* **2017**, *5*, 10266.
[140] X. Wang, G. Tai, Z. Wu, T. Hu, R. Wang, *J. Mater. Chem. A* **2017**, *5*, 23471.
[141] X. Liu, Y. Wang, L. Chen, P. Chen, S. Jia, Y. Zhang, S. Zhou, J. Zang, *ACS Appl. Mater. Interfaces* **2018**, *10*, 37067.
[142] K. Takanabe, *ACS Catal.* **2017**, *7*, 8006.
[143] J. Ran, J. Zhang, J. Yu, M. Jaroniec, S. Z. Qiao, *Chem. Soc. Rev.* **2014**, *43*, 7787.
[144] Y. Yang, C. Sun, L. Wang, Z. Liu, G. Liu, X. Ma, H.-M. Cheng, *Adv. Energy Mater.* **2014**, *4*, 1400057.
[145] L. Li, Z. Deng, L. Yu, Z. Lin, W. Wang, G. Yang, *Nano Energy* **2016**, *27*, 103.
[146] C. Yu, X. Zhang, *ChemElectroChem* **2019**, *6*, 2004.
[147] Y. Yang, M. Wang, P. Zhang, W. Wang, H. Han, L. Sun, *ACS Appl. Mater. Interfaces* **2016**, *8*, 30143.
[148] K. Dang, X. Chang, T. Wang, J. Gong, *Nanoscale* **2017**, *9*, 16133.
[149] Q. Zhu, B. Qiu, M. Du, M. Xing, J. Zhang, *Ind. Eng. Chem. Res.* **2018**, *57*, 8125.
[150] A. Liao, H. He, Z. Fan, G. Xu, L. Li, J. Chen, Q. Han, X. Chen, Y. Zhou, Z. Zou, *J. Catal.* **2017**, *352*, 113.
[151] Y. Yang, Y. Kang, G. Liu, H.-M. Cheng, *Chin. J. Catal.* **2018**, *39*, 431.
[152] J. Huang, J. Chen, T. Yao, J. He, S. Jiang, Z. Sun, Q. Liu, W. Cheng, F. Hu, Y. Jiang, Z. Pan, S. Wei, *Angew. Chem., Int. Ed.* **2015**, *54*, 8722.
[153] X. Zhang, L. Huang, Y. Han, M. Xu, S. Dong, *Nanoscale* **2017**, *9*, 5583.
[154] Y.-J. Tang, C.-H. Liu, W. Huang, X.-L. Wang, L.-Z. Dong, S.-L. Li, Y.-Q. Lan, *ACS Appl. Mater. Interfaces* **2017**, *9*, 16977.
[155] M. Zhou, Q. Weng, X. Zhang, X. Wang, Y. Xue, X. Zeng, Y. Bando, D. Golberg, *J. Mater. Chem. A* **2017**, *5*, 4335.
[156] P. Chen, K. Xu, Z. Fang, Y. Tong, J. Wu, X. Lu, X. Peng, H. Ding, C. Wu, Y. Xie, *Angew. Chem., Int. Ed.* **2015**, *54*, 14710.
[157] X. Xu, Y. Deng, M. Gu, B. Sun, Z. Liang, Y. Xue, Y. Guo, J. Tian, H. Cui, *Appl. Surf. Sci.* **2019**, *470*, 591.
[158] X. Chen, Z. Yu, L. Wei, Z. Zhou, S. Zhai, J. Chen, Y. Wang, Q. Huang, H. E. Karahan, X. Liao, Y. Chen, *J. Mater. Chem. A* **2019**, *7*, 764.
[159] Y. Jiang, Y. Fang, C. Chen, P. Ni, B. Kong, Z. Song, Y. Lu, L. Niu, *ChemElectroChem* **2019**, *6*, 3684.
[160] Z. Li, M. Shao, H. An, Z. Wang, S. Xu, M. Wei, D. G. Evans, X. Duan, *Chem. Sci.* **2015**, *6*, 6624.